Department of Physics and Astronomy
Heidelberg University

Bachelor Thesis in Physics
submitted by

Vincent Leon Spreter

born in Tettnang (Germany)

2000

Realization of Broadband Si_3N_4 Directional Couplers using Partial Euler Bends

This Bachelor Thesis has been carried out by Vincent Leon Spreter at the
Kirchoff Institute of Physics in Heidelberg
under the supervision of
Prof. Dr. Wolfram Pernice

Abstract

Directional couplers (DCs) play an indispensable role in integrated photonics. Thanks to their low loss, they stand as the ubiquitous choice for tasks such as power division and recombination, as well as serving as the fundamental building blocks for interferometry and multiplexing applications. However, conventional DCs suffer from substantial wavelength sensitivity, restricting their bandwidth. This thesis proposes a new directional coupler design on the Si_3N_4 platform to address this limitation. The design presented in this work leverages Euler bends to flatten the wavelength response of the device splitting ratio and minimize losses. The methodology involved simulations employing ANSYS Lumerical©, encompassing finite-difference-eigenmode (FDE) and finite-difference-time-domain (FDTD) solvers. A particle swarm optimization algorithm (PSO) further fine-tunes device parameters. Mach-Zehnder Interferometers (MZI) and cascade structures are fabricated to experimentally characterize the splitting ratio and losses in the near-infrared range, demonstrating directional couplers with 50:50 splitting ratio, a 0.5 dB bandwidth of >160 nm and an overall insertion loss of 0.4 dB in SiN. The method is also applied in a wide range of photonic platforms in addition to SiN such as Si and $LiNbO_3$. Integrating these promises the realization of wavelength-independent architectures with remarkably low losses.

Kurzfassung

Richtkoppeln (DCs) spielen in der integrierten Photonik eine unverzichtbare Rolle. Dank ihrer geringen Verluste sind sie die erste Wahl für Aufgaben wie Leistungsteilung und Rekombination und dienen als grundlegende Bausteine für Interferometrie- und Multiplexanwendungen. Herkömmliche DCs leiden jedoch unter einer erheblichen Wellenlängenempfindlichkeit, was ihre Bandbreite einschränkt. Diese Arbeit schlägt ein neues Richtkopplerdesign auf der Si_3N_4-Plattform vor, um diese Einschränkung zu beheben. Das in dieser Arbeit vorgestellte Design nutzt Euler-Biegungen, um den Wellenlängengang des Teilungsverhältnisses zu glätten und die Verluste zu minimieren. Die Methodik umfasste Simulationen mit ANSYS Lumerical©, die Finite-Differenzen-Eigenmode- (FDE) und Finite-Differenzen-Methode im Zeitbereich (FDTD) umfassten. Ein Partikelschwarm-Optimierungsalgorithmus (PSO) sorgt für die Feinabstimmung der Geräteparameter. Mach-Zehnder-Interferometer (MZI) und Kaskadenstrukturen werden hergestellt, um das Aufspaltungsverhältnis und die Verluste im nahen Infrarotbereich experimentell zu charakterisieren. Dabei werden Richtungskoppler mit einem Aufspaltungsverhältnis von 50:50, einer 0.5 dB Bandbreite von >160 nm und einer Einfügungsdämpfung von insgesamt 0.4 dB in SiN demonstriert. Die Methode wird auch an photonischen Plattformen zusätzlich zu SiN wie Si und $LiNbO_3$ angewendet. Ihre Integration verspricht die Realisierung von wellenlängenunabhängigen Architekturen mit bemerkenswert niedrigen Verlusten.

Contents

1 | Introduction

Integrated photonics is a rapidly evolving field, where light is harnessed and manipulated on a chip-scale platform. This technology leverages the principles of photonic circuitry to enable the integration of various optical components and functions onto a single substrate, akin to the way electronic circuits have revolutionized information processing. By confining and guiding light through waveguides, modulators, detectors, and other passive and active devices, integrated photonics offers unprecedented opportunities for compact, energy-efficient, and high-speed communication, sensing, and signal processing systems. An example of such an active device is the directional coupler (DC), which finds applications in various contexts within integrated photonics.

he focus of this work is on optimizing directional couplers, as conventional DCs suffer from significant wavelength dependence, limiting their bandwidth and consequently, their applications. This work employs countermeasures against this wavelength sensitivity by introducing an asymmetry in the structure of the directional coupler. The goal is to realize a wavelength-independent device, compatible with the typical dimensions used in the research group, operating with minimal losses in the near-infrared range around 1550 nm.

2 | Theory

To understand of the theory behind this work, several concepts from guided wave photonics are outlined. These include the background of the directional couplers, fiber-to-chip coupling with gratings and 3D couplers, as well as the background on Mach-Zehnder interferometers. Furthermore, the background behind simulation and optimization procedure, which is used in this work, is also explained.

2.1 Optical Coupling in Adjacent Waveguides

A directional coupler essentially consists of two waveguides positioned so closely that their evanescent fields overlap. An exact description using Maxwell's equations exceeds the scope of this work, and we turn to a simpler model that, through a few simplifications, provides an adequate description of the coupling process: the coupled mode theory (CMT).

CMT is a fundamental framework used to understand the interaction of optical modes within waveguide structures. It provides a powerful tool for analyzing the transfer of power between adjacent waveguides through mode coupling. CMT enables the prediction of phenomena such as mode conversion, coupling efficiency, and interference effects. This theory underpins the design and optimization of a wide range of photonic devices including directional couplers. The following derivation of the coupled power has been adapted from [1].

In general, the field in a waveguide can be expressed as a superposition of the allowed modes within it:

$$\vec{E} = \Sigma_m a_m u_m(y) e^{-i\beta_m z} \tag{2.1}$$

Here, $a_m(z)$ represents the amplitude of the m-th mode, $u_m(y)$ represents its field distribution and β_m its propagation constant. For our purposes, we will describe the coupling between two adjacent waveguides. These are positioned so closely that portions of the evanescent fields of the modes encompass each other's respective waveguides where we consider, for the sake of simplicity, the coupling between two single-mode slab waveguides with width d and gap d, which is infinitely long in the x-z plane with z being the direction of propagation. The fundamental idea here is that the allowed modes can be described by a superposition of the modes of the individual waveguides (when they are far apart and thus independent). However, this requires that the coupling is not too strong. InCMT, these modes remain unchanged, only their amplitudes are influenced, which makes them vary along the z-direction $a_m(z)$. The coupling

process can be understood as a scattering of the fields from one waveguide to the other. The resulting change in amplitudes can be described using these two partial differential equations:

$$\frac{da_1}{dz}(z) = -ic_{21}e^{i\Delta\beta z}a_2(z) \tag{2.2}$$

$$\frac{da_2}{dz}(z) = -ic_{12}e^{-i\Delta\beta z}a_1(z) \tag{2.3}$$

with $\Delta\beta = \beta_1 - \beta_2$. c_{ij} are the coupling coefficients which relate to the overlap of the field profiles. These are the trial solutions needed:

$$a_1(z) = b_1 e^{i\gamma z}e^{i\Delta\beta z/2} \tag{2.4}$$

$$a_2(z) = b_2 e^{i\gamma z}e^{-i\Delta\beta z/2} \tag{2.5}$$

b_i are constants and γ can be positive or negative;

$$\gamma = \pm\sqrt{\left(\frac{\Delta\beta}{2}\right)^2 + c^2}, \quad c = \sqrt{c_1 2 c_2 1} \tag{2.6}$$

By modifying the trial solution to be superpositions of $sin(\gamma z)$ and $sin(\gamma z)$ while using positive γ we can arrange the solution in following matrix expression:

$$\begin{pmatrix} a_1(z) \\ a_2(z) \end{pmatrix} = \begin{pmatrix} A(z) & B(z) \\ C(z) & A^*(z) \end{pmatrix} \begin{pmatrix} a_1(0) \\ a_2(0) \end{pmatrix} = T \begin{pmatrix} a_1(0) \\ a_2(0) \end{pmatrix} \tag{2.7}$$

T is the transmission matrix,and $a_i(0)$ the boundary conditions. The matrix elements are:

$$A(z) = e^{i\Delta\beta z/2}\left(\mathbf{cos}(\gamma z) - i\frac{Delta\beta}{2\gamma}\mathbf{sin}(\gamma z))\right) \tag{2.8}$$

$$B(z) = \frac{c_{21}}{i\gamma}e^{i\Delta\beta z/2}\mathbf{sin}(\gamma z) \tag{2.9}$$

$$C(z) = \frac{c_{12}}{i\gamma}e^{-i\Delta\beta z/2}\mathbf{sin}(\gamma z) \tag{2.10}$$

If we consider only the input 1 being active then $a_(0) = 0$ follows. Thus, the power $P_i = |a_i(z)|^2$ in each waveguide follows as:

$$P_1(z) = P_1(0)\left[\mathbf{cos}^2(\gamma z) + \left(\frac{\Delta\beta}{2\gamma}\right)\mathbf{sin}^2(\gamma z)\right] \tag{2.11}$$

$$P_2(z) = P_1(0)\frac{|c_{21}|^2}{\gamma^2}\mathbf{sin}^2(\gamma z) \tag{2.12}$$

In these two expressions above, it can be easily seen that for the phase-matched case, such as when symmetric waveguides are present, complete power coupling from 1 to 2 is possible. Subsequently, a coupling length $L_0 = \pi/2c$ can be defined, indicating the distance at which complete coupling occurs. In our case, where a 50:50 splitting is desired, the sinusoidal profile of $P_2(z)$ always has the steepest slope, resulting in high sensitivity to e.g. wavelength. For each wavelength, a different coupling length is required. The goal of this work is to minimize this effect by introducing an asymmetry to flatten the coupled power,

resulting in a decrease in both the peak and the slopeand there the wavelength sensitivity

There are several ways to introduce asymmetry, such as varying waveguide widths or imposing a stronger curvature on one waveguide compared to the other. Both approaches have the drawback of being relatively lossy. Therefore, this work employs partial Euler bends, which mitigate this issue. For further information regarding this topic, refer to [2]

2.2 Simulation and Optimization

This work frequently utilizes the simulation software ANSYS Lumerical™, making it necessary to gain an overview of the numerical solvers used. The Finite-Difference Eigenmode solver (FDE) solver from Lumerical MODE™ as well as Lumerical FDTD were employed. Furthermore, we aim to explore optimization using a particle swarm algorithm (PSO), with an initial guess estimated from the Transfer Matrix Method (TMM).

2.2.1 Finite-Difference-Eigenmode

First, the eigenmodes of the coupling and non-coupling sections are calculated for a specific wavelength range via Lumerical MODE's FDE solver. Then their overlaps are calculated for analyzing the device performance via TMM where we sweep over α and L_s. FDE solves the Maxwell equations of the cross-sectional area perpendicular to the propagation direction of the waveguide completely vectorially based on [4]. The finite-difference algorithm builds a mesh around the cross section to be simulated. Then the Maxwell equations with the simulation's boundary conditions are expressed as an eigenvalue problem whose eigenvalues are β^2. This allows effective index and mode field profiles to be determined, with fields always normalized. Lumerical MODE analysis functions allow the calculation of field overlap and power coupling of two different modes. Mode overlap from mode 2 into mode 1 is described as follows [5]:

$$\mathbf{overlap}(\mathbf{e_1}, \mathbf{e_2}) = \frac{1}{\mathbf{Re}(\int \vec{E}_2 \times \vec{H}_2^* d\vec{S})} \mathbf{Re}\left[\frac{(\int \vec{E}_1 \times \vec{H}_2^* d\vec{S})(\int \vec{E}_2 \times \vec{H}_1^* d\vec{S})}{\int \vec{E}_1 \times \vec{H}_1^* d\vec{S}}\right] \tag{2.13}$$

which can be interpreted as a fractional power coupling. Here, differences in indices and the resulting reflection are not taken into account. To counteract this, the power coupling from the overlap analysis window is used in the actual calculation, which also takes this difference in the indices into account by calculating the Fresnel transmission. For a detailed consideration of the Fresnel transmission, see [5]. Propagation losses can be determined from the imaginary part κ of the effective indices obtained with FDE:

$$a_p = 20\mathbf{log}_10(e)\frac{2\pi\kappa}{\lambda_0} \tag{2.14}$$

λ_0 represents the wavelength in vacuum.

2.2.2 Finite-Difference-Time-Domain Simulation

Finite-Difference-Time-Domain Simulation (FDTD) allows to perform numerical simulations in time domain, which allows effective simulations over a broad range of wavelengths at the same time. The geometry to be simulated is discretized into a mesh in which the time-dependent Maxwell equations are solved numerically. Inside a cell element, the Yee cell, both electric and magnetic fields are determined. The points at which these are calculated are staggered from each other, which has several advantages: At each grid point, the new $\vec{E}$-field and the new $\vec{H}$-field for the next time step are determined alternately in a leap-frog manner. The change of the $\vec{E}$-field is calculated from the numerical rotation of the adjacent $\vec{H}$-field. Vice versa, the change of the $\vec{H}$-field is again calculated from the rotation of the neighboring $vecE$-field.

A major advantage of FDTD is its precision, which makes it possible to simulate arbitrary geometries where an analytical solution would be almost impossible. This makes this method ideal for the device geometry described in this work, whose complicated bending behavior is very difficult to handle analytically without compromising approximations. This precision is at the expense of the limited simulation resources, which is why the FDTD simulations in the particle swarm optimization contain comparatively loose meshes, while the FDTD simulations for the verification of the results are very accurate at the end.

2.2.3 Transfer Matrix Method and Supermodes

The Transfer Matrix Method (TMM) is a versatile technique. TMM serves as a fundamental tool for understanding and optimizing the behavior of light propagation, reflection, and transmission within photonic devices. Each section in an integrated photonic device can be characterized by a transfer matrix, which describes the propagation of modes in each interface. By cascading these matrices for multiple sections, the overall transfer matrix of the entire device can be constructed, allowing for a comprehensive understanding of the light's behavior.

This method can also be applied here in a similar way to the procedure for constructing the transfer matrix in [7]. However, this works only by applying some simplifications of the geometry: a circular curvature like in [7] is assumed, thus the Euler bend is ignored. In addition, possible coupling at the input and output waveguides leading to and away from the straight sections has not been taken into account. An exact modeling of the Euler bends by TMM is beyond the scope of this work. Taking these key assumptions and only the first two supermodes into account, the following transfer matrices for propagation can be set up for the each individual sections of the DC:

$$P_{ss} = \begin{pmatrix} e^{i\beta_{ss,1}L_s} & 0 \\ 0 & e^{i\beta_{ss,2}L_s} \end{pmatrix} \tag{2.15}$$

Propagation transfer matrix for the curved section:

$$P_{cs} = \begin{pmatrix} e^{2i\beta_{cs,1}\pi\alpha} & 0 \\ 0 & e^{2i\beta_{cs,2}\pi\alpha} \end{pmatrix} \tag{2.16}$$

These matrices describe only the propagation of the supermodes 1 and 2 that are allowed in the respective section. To effectively describe the coupling of these supermodes between two different sections, two coupling matrices are required, in which the amplitude overlaps of the corresponding supermodes are entered. The coupling matrix from the single input waveguides into the straight coupling section is described as follows:

$$C_{s,ss} = \begin{pmatrix} \mathbf{e_{s1}} \cdot \mathbf{e_{ss1}} & \mathbf{e_{s2}} \cdot \mathbf{e_{ss1}} \\ \mathbf{e_{s1}} \cdot \mathbf{e_{ss2}} & -\mathbf{e_{s2}} \cdot \mathbf{e_{ss2}} \end{pmatrix} \tag{2.17}$$

The Coupling matrix from the straight coupling section into the curved section:

$$C_{ss,cs} = \begin{pmatrix} \mathbf{e_{ss1}} \cdot \mathbf{e_{cs1}} & \mathbf{e_{ss20}} \cdot \mathbf{e_{cs1}} \\ \mathbf{e_{ss1}} \cdot \mathbf{e_{cs2}} & -\mathbf{e_{ss2}} \cdot \mathbf{e_{cs2}} \end{pmatrix} \tag{2.18}$$

$\mathbf{e_i}$ represents the respective supermode, $\mathbf{e_i} \cdot \mathbf{e_i}$ the amplitude coupling from mode i into mode j. which is described as the amplitude overlap between these two:

$$\mathbf{e_i} \cdot \mathbf{e_j} = \mathbf{Re}\left[\frac{\int \vec{E}_i \times \vec{H}_j^* d\vec{S} \int \vec{E}_j \times \vec{H}_i^* d\vec{S}}{\int \vec{E}_i \times \vec{H}_i^* d\vec{S} \int \vec{E}_j \times \vec{H}_j^* d\vec{S}}\right]^{\frac{1}{2}} = \sqrt{\mathbf{overlap(e_i, e_j)}} \tag{2.19}$$

As one can see above, the overlap analysis from Lumerical MODE can be used to find the amplitude overlap and thus the coupling matrices. Amplitude coupling is independent of the order whether mode 1 excites mode 2 or vice versa:

$$\mathbf{e_i} \cdot \mathbf{e_j} = \mathbf{e_j} \cdot \mathbf{e_i} \implies C_{i,j} = C_{j,i}^T \tag{2.20}$$

This implies that for the reversed propagation the transposed coupling matrix can be used. For the entire DC, the following transfer relation can now be used, which takes all sections into account:

$$\begin{pmatrix} A_{1,out} \\ A_{2,out} \end{pmatrix} = C_{s,ss}^T P_{ss} C_{ss,cs}^T P_{cs} C_{ss,cs} P_{ss} C_{s,ss} \begin{pmatrix} A_{1,in} \\ A_{2,in} \end{pmatrix} \tag{2.21}$$

A_i describes the amplitude of the i^{th} supermode, e.g. $A_{1,in} = 1$ and $A_{2,in} = 0$ would mean that only supermode 1 is injected. It is now possible to obtain the output intensity via $I_{i,out} = |A_{i,out}|^2$ and thus the cross power splitting ratio:

$$\eta_c = \frac{I_c}{I_b + I_c} = \frac{|A_c|^2}{|A_b|^2 + |A_c|^2} \tag{2.22}$$

With A_c being the amplitude of the cross single output mode and A_b corresponding to the bar waveguide. The method can only be applied to one wavelength at once. In order to examine the full bandwidth, the amplitude overlaps would have to be determined for each wavelength individually, which would require an excessive amount of resources. Therefore, the overlaps are determined via FDE only at some specific wavelengths, e.g. 1550 nm, and at the ends of the range under investigation, the intermediate ranges are linearly interpolated. This loss of precision between interpolation points is tolerable since 1550 nm is of primary interest and the determining of the largest deviation from this value is only slightly affected by this limitation compared to the previously mentioned approximations (circular bend and no coupling at the input and output waveguides).

Now the parameters can be swept over and corresponding candidates can be found. The parameters we gained in this way are now used as the initial guess for the optimization procedure.

2.2.4 Particle Swarm Optimization

Particle Swarm Optimization (PSO) is a computational optimization technique inspired by the collective behavior of social organisms, such as flocks of birds [8].

Here, a population of candidate solutions, here referred to as particles, is moved through a search space. In each iteration step, the positions of the particles are updated. Each of the individual particles has a position $\vec{p}$ a velocity $\vec{v}$ vector, an inertia ω, a memory for the individual best coordinates $\vec{p}_{best}$, a cognitive weight factor c_c, and a social weight factor c_s. Each particle knows the global best coordinates $\vec{g}_{best}$ which was found so far. The velocity of the i^{th} particle in the next step is then composed as follows [9], [10]:

$$\vec{v}_i(n+1) = \omega\vec{v}_i(n) + c_c r_1(\vec{p}_{i,best} - \vec{p}_i(n)) + c_s r_2(\vec{g}_{best} - \vec{p}_i(n)) \tag{2.23}$$

$$\vec{p}_i(n+1) = \vec{p}_i(n) + \vec{v}_i(n+1) \tag{2.24}$$

where r_1 and r_2 represent random numbers within an interval of $[0, 1]$. In addition, an initial start position $\vec{p}(0)$ can be selected, which in our case corresponds to the point of interest obtained from the TMM, the initial velocities $\vec{v}_i(0)$ are randomly chosen. To prevent premature convergence at a local minimum, the weight factors can be chosen adaptively. To counteract a possible divergence of the particles the inertia must be $\omega < 1$. Moreover, it is common to set an upper limit for the velocity parameters [11].

The biggest advantage of PSO for this work is that it does not need gradients to be calculated and therefore only the result of the figure of merit (FOM) is required. This also means that, in contrast to e.g. gradient descent methods, the function of the problem does not have to be differentiable. For each individual particle, a FDTD simulation is performed: the DC geometry is generated and simulated with the coordinate of the respective particle in the search space. The simulation yields the cross port power splitting ratio η_c over the wavelength range of interest. The figure of merit in this work of whose minimum is to be found is composed as follows:

$$\mathbf{FOM} = |\eta_c(1550\mathbf{nm}) - 0.5| + \Delta\eta_c \tag{2.25}$$

$$\Delta\eta_c = \mathbf{max}|\eta_c(1550\mathbf{nm}) - \eta_c(\lambda)| \tag{2.26}$$

The first term considers the deviation of η_c at wavelength 1550 nm from the ideal target of 0.5, while the second term represents the maximum deviation of η_c in the wavelength range under investigation compared to η_c at 1550 nm. It is also possible to weight the individual terms with their own factors or to add addiotional terms to be minimized, e.g. the insertion loss (IL), ideally aiming for a value of zero dB:

$$a_I = -10\mathbf{log}_{10}\left(\frac{I_{out}}{I_{in}}\right) \tag{2.27}$$

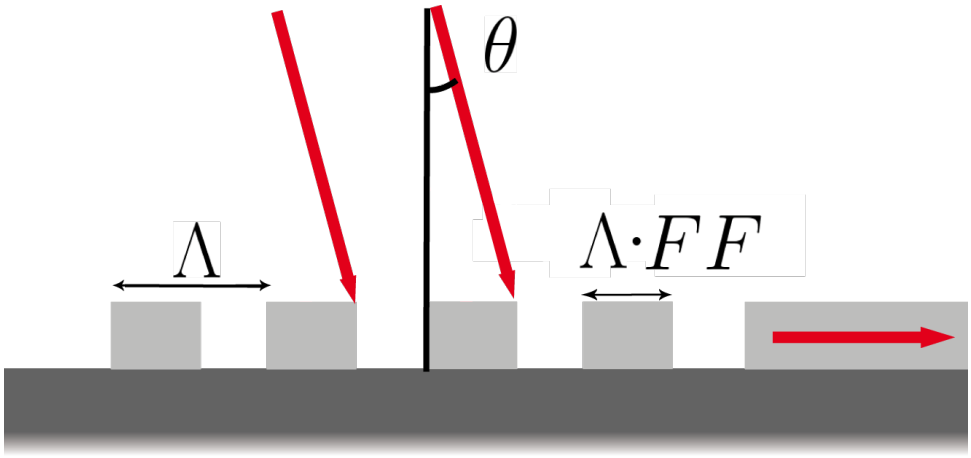

Figure 2.1: Schematic cross-section of a grating coupler. Light is emitted through a fiber array. Arriving at the correct angle, the diffracted light couples into the waveguide.

Incorporating the insertion loss into the fom prevents the scenario of zero transmission through the device. A transmission of zero at both outputs represents a perfect 50:50 splitting ratio and wavelength independence while being essentially non-functioning.

2.3 Grating and 3D Coupler

For the measurements in this work, finding effective ways to couple light from a laser into the chip's structures is crucial. Two components that can achieve this are the grating coupler and the 3D coupler. In this section, we briefly describe the physical principles underlying these components and then assess their capabilities and limitations.

Grating Coupler

The device consists of a periodic grating structure etched onto the surface of the waveguide. When light from an optical fiber is incident on the grating, the periodic structure causes the light to diffract into various angles. Some of this diffracted light is coupled into the waveguide, effectively transferring the optical signal from the fiber to the chip. The specific design of the grating, including its period, depth, and pitch, is crucial for optimizing the coupling efficiency and matching the optical modes between the fiber and the waveguide.

n this case, there are two requirements: firstly, efficient coupling should be achievable, and secondly, it should have a wide bandwidth. Figure 2.1 examines the cross-section along the propagation direction (Figure **??**) clarifies the operational principle. The rectangles represent the same material as the waveguides, arranged periodically. The period length is denoted as Λ, and the fill factor F indicates the ratio of the period's material fill. Similar to the conventional Bragg diffraction in crystals, light entering from the top is diffracted by the

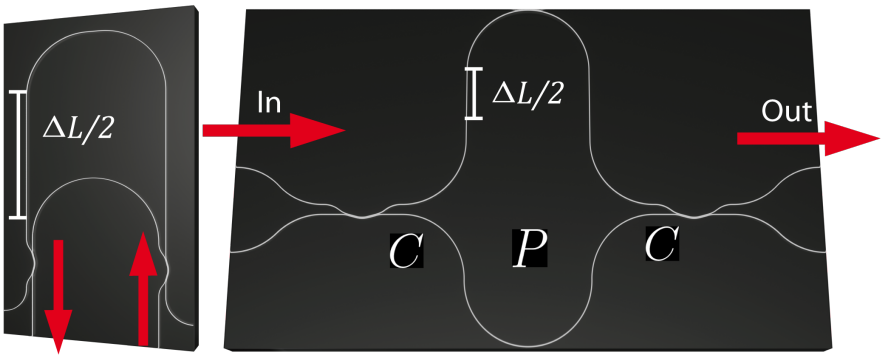

Figure 2.2: Here are the two types of MZIs used in this work. On the left is the more compact MZI used in the last measurement with the 3D couplers. On the right, you can also see the section markings as discussed in the theoretical treatment.

grating into directions that satisfy the Bragg condition [3]:

$$\Lambda \mathbf{sin}\theta + \Lambda \mathbf{sin}\theta' = n\lambda \tag{2.28}$$

with n being a natural number and θ being the angle of the incident and θ' diffracted light.

3D Coupler

Given that grating couplers have a limited bandwidth due to coupling through diffraction, and measures to increase this bandwidth can reduce efficiency, an alternative type of coupler can be used, which couples light into structures through refraction. In principle, this component can be visualized as a lens whose geometry refracts light from a broader range of wavelengths into the waveguides. The use of 3D couplers also comes with disadvantages. The geometries are printed onto the chip with the highest precision, yet alignment issues frequently arise. Moreover, this printing process is relatively slow; fabricating a 3D coupler takes approximately 15 minutes, significantly limiting the number of 3D couplers that can be employed. Additionally, the fabrication imposes specific requirements on the chip that grating couplers do not have, such as cladding-free windows.

2.4 Mach-Zehnder Interferometer

An important device to test the performance of the directional coupler is the Mach-Zehnder interferometer. In this work, the MZI holds a crucial position, making it important to understand its physical background.

A MZI essentially comprises two beam splitters, in our case, the directional couplers. One of the split beam paths undergoes a longer optical path than

the other with the difference $\Delta L = L_2 - L_1$. The two paths meet at the second directional coupler, resulting in the interference of the recombined light. Here, we can represent the propagation of amplitudes starting from $(\epsilon_{1,in}, \epsilon_{2,in})$ through the individual sections of the MZI using transfer matrices. ϵ_1 represents the amplitude of the light in the upper while ϵ_2 the light in the lower waveguides:

$$\begin{pmatrix} \epsilon_{1,out} \\ \epsilon_{2,out} \end{pmatrix} = CPC \begin{pmatrix} \epsilon_{1,in} \\ \epsilon_{2,in} \end{pmatrix} \tag{2.29}$$

where

$$C = \begin{pmatrix} \sqrt{1-\eta_c} & i\sqrt{\eta_c} \\ i\sqrt{\eta_c} & \sqrt{1-\eta_c} \end{pmatrix}, \; P = \begin{pmatrix} e^{-a\Delta L/2} e^{-i\beta\Delta L} & 0 \\ 0 & 1 \end{pmatrix} \tag{2.30}$$

C is the coupling matrix for the couplers an P the propagation matrix. For interference, only the relative phase difference caused by the path imbalance matters. Approximately, the directional couplers here are treated as symmetric. If we neglect the loss experienced by the light in the longer arm (the upper one) And if we inject only Input 1 for this scenario, the amplitude at output 1 follows:

$$\epsilon_{1,out} = -\eta_c e^{-i\beta\Delta L} \epsilon_{1,in} + (1-\eta_c)\epsilon_{2,in} \tag{2.31}$$

This results in the following intensity:

$$I_{1,out} = |\epsilon_{1,out}|^2 = 2\eta_c^2 - 2\eta_c + 1 - 2\eta_c(1-\eta_c)cos(\beta\Delta L) \tag{2.32}$$

The extinction ratio, which we will measure in this work, is them defined as follows:

$$\mathbf{ER} = \frac{I_{max}}{I_{min}} = \frac{1}{4\eta_c^2 - 4\eta_c + 1} \tag{2.33}$$

Substituting $1/\mathbf{ER}$, you obtain a quadratic equation, which can be easily solved for η_c. Resubstitution yields:

$$\eta_c = \frac{1}{2} \pm \frac{1}{\sqrt{\mathbf{ER}}} = \frac{1}{2} \pm \frac{1}{10^{\mathbf{ER}_{dB}/5}} \tag{2.34}$$

Since we obtain $\mathbf{ER}_{dB}$ directly from the measurement by subtracting the minima powers from the maxima (dB). The uncertainty of η_c is calculated as follows:

$$\Delta_{error}\eta_c = \frac{ln(10)}{5} 10^{-\mathbf{ER}_{dB}/5} \Delta\mathbf{ER}_{dB} \tag{2.35}$$

Conclusion

In this section, we obtained an overview of the fundamentals of coupled mode theory to describe a directional coupler. We determined that for a broader bandwidth, the coupled power needs to be flattened, allowing the peak to be close to the desired 0.5 and reducing the steepness of the slope, which can be realized by adding a mismatch between the propagation constant through e.g. bending. We then delved into the fundamentals of optimization and simulation employed in this work. Lastly, a component that plays a particularly important role in this thesis, the MZI, was investigated. Here, we explored how the power splitting ratio can be determined from the measured extinction ratios With this theoretical framework in place, we are now equipped to conduct the optimization

process and understand the crucial parameters for measurement to obtain the power splitting ratio. Now, let's delve into the specific methods that have been employed.

3 | Methods

In this chapter, we examine the methods employed in this study. We explore the design of the directional coupler, along with optimization strategies for its parameters determining the device's behavior and the requirements they must meet within the contexts in which they are employed. Additionally, we investigate how the experimental setups used for performance measurement operate, discuss how performance is defined in which context and explore the required nanofabrication procedure and its tools.

3.1 Design Principle

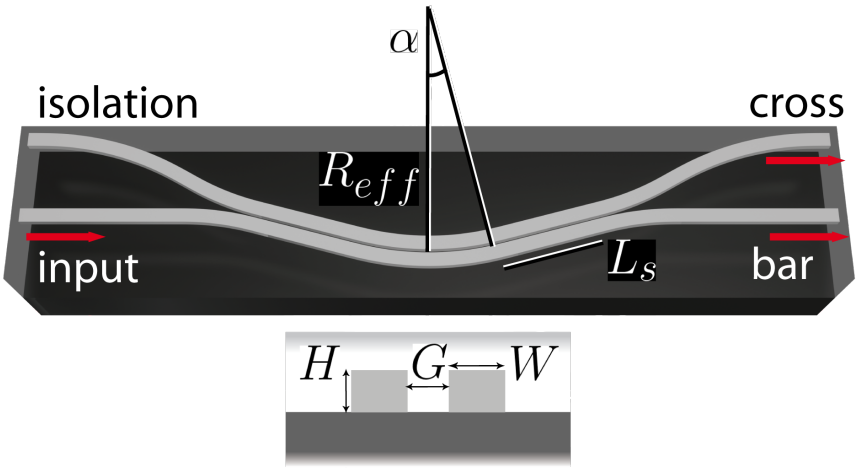

Figure 3.1: Design of the asymmetric directional couplers (DC) characterized by two straight and one Euler bent coupling section.

The basic configuration of a directional coupler consists of two parallel ridge waveguides, which allow the coupling between the propagating modes. The optimized devices realized in this thesis contain a curved and two straight sections characterized by the bend angle α and length L_s respectively (Figure 3.1). The bending corresponds to a partial Euler curvature characterized by the ratio of Euler to circular bending p and the effective radius R_{eff}. G is the distance between the waveguides, W their width and H their height.

The objective of integrating the optimized DCs into established platforms and meeting the experimental demands constrains the thickness H depending on the material platform. W should roughly match the commonly used widths for single mode operation, the device operates in single mode exclusively. In this case, W is consistently greater than the H, favoring the propagation of TE-like modes due to lower losses, making them preferred over TM.

3.2 Simulation and Optimization Procedure

The optimization procedure in this work follows four main steps:

1. calculation of the supported eigenmodes using Finite-Difference-Eigenmode (FDE)
2. finding optimal α and L_s with the Transfer matrix method (TMM)
3. running Finite-Difference-Time-Domain (FDTD) optimization using a particle swarm algorithm with the previously found parameters as an initial starting point
4. verifying the result with an exact FDTD simulation

In the following sections, we will delve into how and in what manner the previously mentioned steps have been precisely employed, along with the rationale behind their usage.

Before starting a simulation, material properties, simulation region and geometry have been selected. Port 3 at the bottom left serves as input, where the profile of the fundamental TE mode was determined at the beginning. Since broadband simulations are intended, the modes are calculated at different frequency points within the wavelengths to be simulated in a Chebyshev distributed manner, characterized by the number of frequency points. The reason for this is to minimize the error due to mode mismatch between calculated and allowed modes if the mode profile had only been determined at one frequency point otherwise. In this way, the modes actually injected in the simulation can be calculated comparatively precisely via interpolation on the Chebyshev grid.

To determine the right trade-off between the resources needed for the simulation and the accuracy, convergence testing can be applied.

3.3 Chip Design using GDSHelpers

For nanofabrication, chip designs must be in GDSII file format before other file formats are generated from it for electron beam lithography (EBL). To create these, the GDSHelpers package is used in this work, which enables python scripts to export various structures and geometries into the desired file format. In GDSII (graphic design system II) the layers to be fabricated are saved in a binary format in a hierarchical order. Since this format is rather old, it comes with some disadvantages, such as high memory requirements per file and a limit of 200 points per polygon, which is why more complex geometries have to be broken down into smaller polygons.

Simulation region			
mesh accuracy	4 (PSO), 8 (exact)		
Gap mesh (exact) [nm]	dx =25, dy =10		
No. of freq. points	10 (PSO), 20 (exact)		
sim. range [nm]	200 (PSO), 300 (exact)		
bound. cond.	PML		
input mode	fundamental TE		
n_{clad} @1550 nm	1.44 [12] (PSO), 1.38 [18] (exact)		
Materials	**SiN**	**SOI**	**LNOI** (x-cut)
n_{core} @1550 nm	1.99 [13]	3.47 [12]	n_x =2.21, $n_{y,z}$ =2.14 [14]
Height H [nm]	330	220	300
Width (top) W [μm]	1.1	0.5	1.1
Gap G [nm]	300	100	400
Base angle θ [°]	90	90	62

Table 3.1: Parameters used for FDTD simulations. The meshing type is conformal variant 0 and boundary conditions are PML for both. Values for n are @1550 nm.

GDSHelpers is based on shapely, a package made for manipulation and analysis of planar geometric objects in python [16]. With GDSHelpers it is possible to convert shapely objects into gdspy as well as gdsCAD objects and export the designs as GDSII. With the fatamorgana package it is also possible to export to the more recent OASIS format, which has significant advantages over GDSII. For detailed information on how gdshelpers operates, refer to the following publication: [15].

The same script that was used for FDTD before generates the device geometry from the specified parameters, which has been added as a function to the parts library of gdshelpers.

The size of the chips used is 15×15 $\mathbf{mm^2}$ with a maximum writing area of 12.8×12.8 $\mathbf{mm^2}$. On these, different structures have been sweeped over, i.e. the same structure, but with different parameters of the DC. Among the structures are MZIs, cascade structures, racetrack resonators and calibration structures for, among other uses, alignment. Markers and labels have also been added for better orientation.

3.3.1 Mach-Zehnder Interferometers

From the extinction ratios (ER) of the Mach-Zehnder interferometers (MZIs), as discussed in the theoretical chapter, the power splitting ratios can be determined. In this case, two DCs are employed as MZIs, with their arms interconnected, where one arm is 300 μm longer than the other (Figure 4.4). The goal is to achieve a Free Spectral Range (FSR) of approximately 5 nm. This would ensure an adequate number of maxima and minima with simultaneously good resolution. Both arms undergo the same amount and geometry of bends, thereby preventing errors of the ERs. The lower left port serves as the input, and the lower right port of the second DC serves as the output. A closer proximity of the ports minimizes alignment errors during measurement with the fiber array, which is why input and output waveguides have been curved towards the

GCs.

Broadband MZI using 3D couplers

For measuring the broadband behavior, a modified version of the initial design was implemented in the final chip. In this case, the path difference is increased to 600 μm, which is twice as large, and instead of using GCs, 3D couplers are employed to fully utilize the tunable laser's bandwidth spanning from 1480 to 1640 nm. This design is significantly more compact than the first one, although it utilizes only two ports. The structure fits within a write field, preventing stitching errors. Additionally, tapers have been added to both remaining ports (on the spirals) to prevent potential back-reflections. Unlike the first MZI, the DCs are reversed to each other. Due to the asymmetry of the DCs, altered splitting ratios could occur at the edges of the measurement range, enabling an intriguing comparison with the previous MZIs where DCs. In this work, such MZIs have been realized using both regular GCs and 3D couplers.

3.3.2 Cascaded Directional Couplers

Cascaded DCs arranged in series are used to determine losses per device. This is achieved by measuring ports 1-4, whose loss in dB increases linearly by port. From the slope of this line and the power splitting ratio, the insertion loss of an individual DC can be determined. The structures are designed with five outputs, the first four spaced at distances of 127 μm, connected to the cross port outputs of the DCs and the fifth at 254 μm, connected to the bar port output of the fourth DC (Figure 4.10a).

To mitigate the impact of the input and output bends of the DCs, the structure is designed such that the transmission through ports 4 and 5 undergoes an equal number of bends. However, due to its dimensions (2500 by 1500$\mu\mathbf{m}$), fabricating this structure poses a challenge, as there is a risk of stitching errors that could disrupt the ratios of output transmissions, rendering the linear fit meaningless. To address this issue, the cascade structures are assigned to distinct GDS layers. This results in an improved alignment of write fields during the fabrication process.

3.3.3 Grating Coupler Calibration Structures

GC test structures allow for fiber array calibration and an estimation of their losses (neglecting losses in the waveguide). In this study, two different GCs for SiN were utilized, with parameters identical except for the opening angle (160° and 180°). The design is kept as simple as possible. There are only two GCs spaced 254 μm apart, equivalent to two port distances of the fiber array. The radius of the semicircle is exactly this distance (127 μm).

3.4 Nanofabrication

All fabrication steps for producing the structures used in this work were conducted at the Münster Nanofabrication Facility (MNF). Creating nanostructures demands utmost precision, meticulous execution, and a profound understanding of the process steps, which exceed the scope of this work. Therefore,

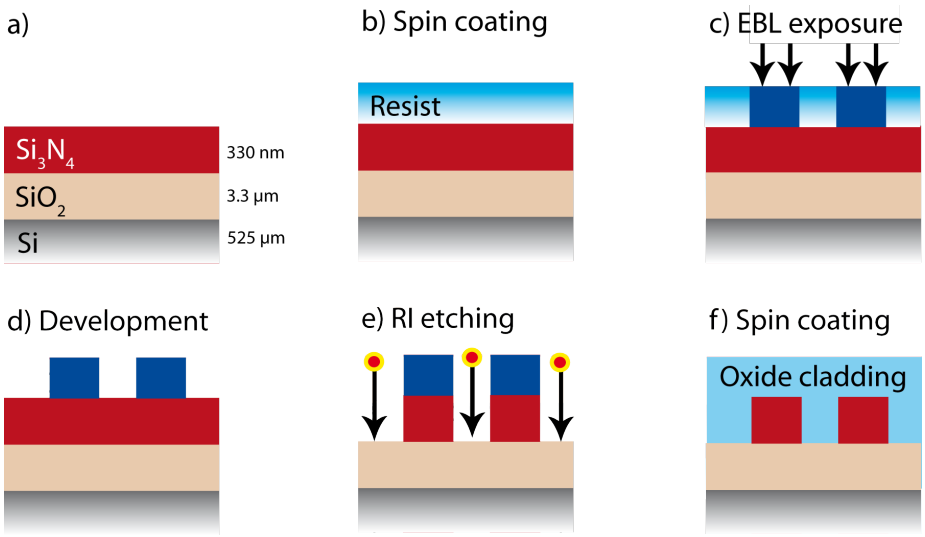

Figure 3.2: a) The wafer is composed as follows: 330**nm** Si_3N_4 on 3.3μ**m** SiO_2 stack on a silicon substrate, b) spin-coating of the resist, c) EBL exposure, d) developnig by the removing unexposed resist, e) reactive ion etching (RIE), f) spin-coating and curing of HSQ to obtain a SiO_2-like cladding.

the fabrication was entrusted to colleagues (see acknowledgments). The subsequent sections briefly outline the necessary fabrication steps.

3.4.1 Electron Beam Lithography

All structures in this work have been fabricated with Electron Beam Lithography (EBL) since one of the advantages of this maskless process is its precision, but at the expense of extended writing times. The principle behind EBL is that 2D structures are etched on a wafer after the structure is written on the electron-sensitive resist on top of the wafer with the electron beam.. The manufacturing process essentially follows a few steps which are discussed in the following section.

First, the resist is spin-coated onto the wafer surface. This ensures an uniform distribution of the resist thickness on the wafer. Then a precisely dosed electron beam writes the structures on the resist, which changes its chemical properties, e.g. its solubility when exposed. In the following step, a solvent (developer) removes the non-exposed resist leaving only the desired structures as resist on the wafer. Finally, the structures are etched into the wafer by dry or wet etching, in which the structures protected by them resist are not affected.

For the purposes of this study, a wafer featuring a stack of 330 nm Si_3N_4 on 3.3 μm SiO_2 on a 525 μ**m** silicon substrate, serves as the initial material for the process. After cleaning with acetone and IPA in a sonicator and annealing for four hours at 1200 °C, the 300 nm thick SX AR-N AR-N 7520.12, a negative resist based on PMMA, is deposited on the surface via spin-coating for one minute at a speed of 2000 rpm. The next step involved EBL exposure with EBPG5150 from the manufacturer Raith at a dose of 1400 μC/cm^2. After

the post-exposure bake (PEB), the developer MF-319, a TMAH-based solution, is used for cleaning the unexposed resist away. The dry etching is then performed using reactive ions (RIE) with the Oxford Instruments PlasmaPro 80 RIE system with an etch rate of 63 nm/min. RIE is highly anisotropic and uses a plasma of oxygen and fluoroform (CHF_3) here. Finally, the resist is then stripped away using with oxygen plasma.

3.4.2 Cladding Deposition

Hydrogen silsesquioxane (HSQ) is spin coated onto the wafer surface and then cured to form a SiO_2-like oxide with a comparable refractive index. HSQ's excellent gap-filling and self-planarization properties makes it an ideal material for overcladding nanostructures. Additionally, HSQ can be patterned with high resolution using EBL [17].

Before being cured, it possesses a mixed cage-network structure. The ratio of these two types significantly influences the material's properties, which is why the influence of the curing process (time and temperature) has been thoroughly investigated [18]. It has been demonstrated that the resulting refractive index of the cured oxide decreases with increasing process temperature and the nanopores formed by the gaseous byproducts, cage-network transformations and remaining solvent during curing can largely be held responsible for this effect.

In this study, HSQ with a thickness of 0.8 mum is deposited using spin coating and cured at a temperature of 450°C (vitrification). Subsequently, annealing was carried out at 250°C to evaporate the solvent.

Now that nanofabrication is complete, the focus shifts to examining its results. This step can essentially take place during fabrication or, in our case, before cladding is applied. In the next section, we will explore a method for rapidly generating images with nanometer resolution.

3.5 Scanning Electron Microscopy

Scanning Electron Microscopy (SEM) is a powerful imaging technique that uses a focused electron beam to examine the surface properties and topography of samples at nanoscale resolutions. Interaction between the electrons and the sample generates various signals, including secondary electrons (SE), backscattered electrons (BSE), and X-rays, which are then detected to generate the images. For more detailed information, see [19] SEM is crucial in this context, as it enables us to rapidly generate images and examine the sample in real-time.

In this work, a Microscope of the GeminiSEM series from the manufacturer ZEISS has been used to inspect the fabrication quality of the structures. The samples are placed inside a vacuum chamber along with a sample holder after putting it on a sticky carbon pad. Alternatively, a silver-based adhesive can also be used. At the beginning, the sample is brought into the focus of the electron beam, and astigmatism is corrected if the beam spot is not symmetric. In this case, dirt particles are particularly suitable, as they exhibit a wide range of feature sizes, providing suitable test images for calibration.

Special attention must be paid to the grating couplers, as these have the smallest feature sizes and any problems due to fabrication will quickly become

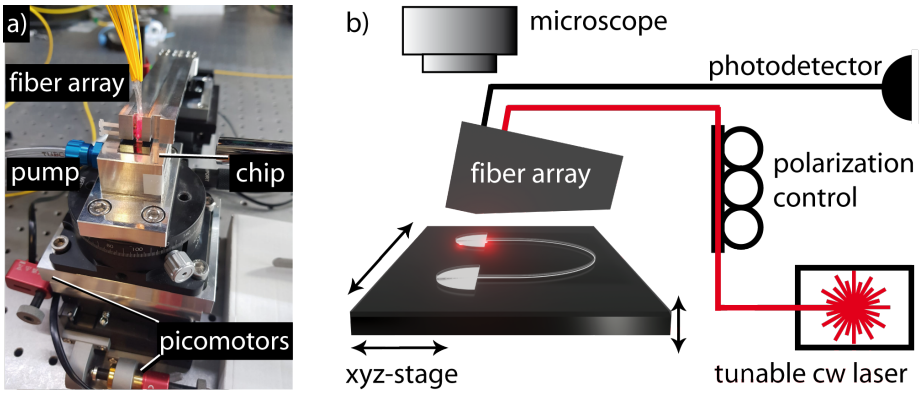

Figure 3.3: Experimental setup, a) setup on the optical table, b) sketch of the measurement procedure.

apparent here. The examination of the surface of the waveguides is also of crucial interest: their roughness has a significant impact on their losses.

3.6 Experimental Setup for Characterization

Now, we aim to test the fabricated structures for their photonic properties. To achieve this, we require a method to couple light from the laser into the structure and out to the photodetector. This is achieved here through a fiber array, a one-dimensional collection of waveguides in an array. Along with the grating couplers in the structures, this enables the coupling of light in and out.

The manufactured devices have all been measured using a fiber array (Figure 3.3). Here, the chip to be examined is suctioned on a motorized stage that can be moved in all spatial directions via picomotors. The position can be controlled manually as well as by a computer. The used fiber array has 16 ports which can be used for input or output coupling. The individual ports are located at a distance of 127 μm from each other on the underside of the array and can be connected individually to different devices. In this case, a tunable laser in connected to the fiber array as input, and a polarization control unit has been set up between the laser and the fiber array. To couple light from the input port into the structure, grating couplers are used, where the array must have the proper position, distance angle over the grating couplers to couple light in. The light coupled from the output grating coupler into the fiber array is directed to a photodetector (PD), which in turn is connected to the computer. To control the position, a optical microscope is attached which is connected to the computer by means of a camera.

The tunable laser TSL-770 used here, manufactured by Santec, enables wavelength sweeps from 1480 nm to 1540 nm. Due to the limited bandwidth of the grating couplers, sweeps from 1500 nm to 1600 nm are mainly used.

Photodetectors of type 2011-FC, manufactured by Newport, enable measurement of transmitted power in a range from 900 nm to 1700 nm. The InGaAs photodiode is connected via a fiber optic cable to ports of the fiber array. The detector unit also offers amplification up to a gain factor of 30000.

3.6.1 Measurement Procedure

For optimal measurement, the test structures and the fiber array must be correctly positioned in relation to each other in order to minimize coupling losses. This is done at the beginning of each measurement series and follows always the same pattern. First, the fiber array is brought over a calibration structure with the help of an alignment laser, which operates in the visible range. With the help of straight lines on the chip, the platform can now be rotated so that the grating coupler and the fiber array become parallel to each other. While the transmission is measured constantly, the actuators of the stage are controlled and the platform is moved in the x-y plane until a local maximum of the transmission is reached. The z-position of the stage is then optimized and the polarization control unit is set so that only TE mode is present. This process is iterative, meaning that the stage is moved along one axis to reach a local optimum and then repeated along another axis, and so forth. Once the maximum transmission is reached, the transmission spectrum of the calibration structure is recorded for later comparison with the transmission spectra of the test structures. This setting is now maintained over the entire series of measurements in order to keep the comparison of the test structures with each other as little affected as possible.

Since for some test structures, such as the MZI, it is important to accurately resolve both transmission maxima and minima in the spectrum with as little noise as possible for the determination of the extinction ratios (ER), in this case both a spectrum with a low gain setting for resolving the maxima and a second spectrum with a high gain setting for resolving the minima are recorded. The spectrum for the minima resolves them accurately, but is oversaturated for the rest of the spectrum. This is solved by merging the two spectra: a saturation level is determined with the help of the minima spectrum and this spectrum is combined with the spectrum of the maxima at all oversaturation wavelenghts so that both minima and maxima are combined in the new spectrum with low noise.

Conlusion

In summary, the methods employed here can be categorized into three distinct sections: Optimization, Design, and Measurement Techniques. After an initial estimation using TMM, a PSO algorithm optimizes the parameters α and L_s through FDTD simulations. Once an optimum is achieved, chips are fabricated using EBL on which sweeps over these parameters are performed with MZIs and cascade structures. Conclusions about the performance of the DCs, primarily η_c and its wavelength dependency, are drawn from their transmissions. These transmissions are then measured using a fiber array, enabling the coupling of light from the tunable laser into the structure and the collection of emitted light from the structures to the photodetector. We will explore the results of these measurements in the following section.

4 | Results

Now, we turn our attention to the outcomes of this study. The results can also be categorized into three parts: optimization, chip design, and structure measurements. First, we will explore the initial guess obtained from the TMM via eigenmodes obtained with FDE and then we discuss the PSO results. After that, we will go over the actual fabricated structures and examine their surface with SEM and discuss observed defects. Finally, we will look at the actual performance, especially the power splitting ratio, and compare it with the simulations.

4.1 Simulation

4.1.1 Effective Radius and Width

The thickness H of the fully-etched SiN waveguides is fixed at 330 μm. The intention is to use the fully etched structures with a SiO_2-like oxide cladding made from cured HSQ. The gap G measures 0.3 μm. These parameters consider fabrication constraints, allowing tolerance for potential manufacturing errors while remaining consistent for SiN.

Using this information, the waveguide's cross section can now be geometrically defined in Lumerical MODE for the FDE solver. SiO_2 serves as a first approximation cladding, with its refractive index in the near-infrared range taken from Palik et al.'s data [12]. For SiN, Luke et al.'s data was used [13]. Since radiative loss occurs in the curved regions, PML boundary conditions must be used. The determination of the modes was not trivial, since the correct guess of the κ for the FDE solver was required. This has been solved by first calculating the mode with small κ, namely the one without curvature, and from there increasing the curvature step by step. Equation 2.14 enables the determination of propagation loss a_P from κ.

n_{eff}, imaginary index κ (and thus the losses), the power couplings at different radii have been determined (Figure 4.1a). The width W has been set to $1.1\mu\mathbf{m}$, providing sufficient mode confinement, hence low propagation losses, while still offering adequate coupling and slope n_{eff}. According to Coupled Mode Theory (CMT) the propagation constants for the two waveguides on the bend coupling section have to be as different as possible to flatten the wavelength dependence (see theory chapter). Since Euler bends are to be used, it needs to be taken into account that these have a slightly increased curvature for the same size than their circular counterparts, which is why an effective radius of $R_{eff} = 40$ μm is chosen here. The Euler bend parameter p has been

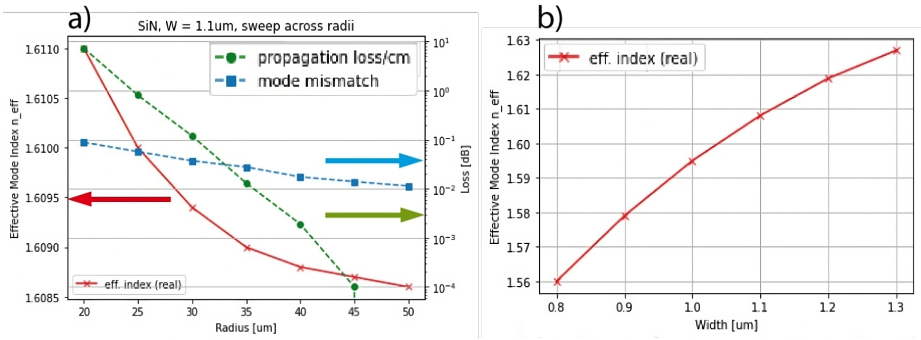

Figure 4.1: Obtained via FDE: a) Sweeping across various radii: effective index (red), mode match (blue), and propagation losses (green) at 1.1 μm. b) Effective index variation with different widths.

set to 0.2, which is derived from the work of Vogelbacher et al. [20] for TE-like modes, although with different wavelengths and waveguide geometry, but in a first approximation this difference is not expected to be significant. The aforementioned parameters for the device geometry are maintained for SiN and summarized in Table 3.1.

4.1.2 TMM

The supermode profiles (Figure 4.2), their overlaps and propagation constants were determined for wavelengths ranging from 1450 to 1650 nm in 50 **nm** increments. The overlaps are linearly interpolated for their use in TMM. Using the thus calculated transfer matrices, the cross power splitting ratio η_c at 1550 **nm**, along with its largest deviation $\Delta\eta_c$, is then determined for various values of α and L_s, yielding a preliminary optimized outcome as a result (Figure 4.3):

$$\alpha_{TMM} = 15.6°, \quad L_s^{TMM} = 13.2\mu\mathbf{m} \tag{4.1}$$

4.1.3 Optimization

The acquired parameters are now utilized as an initial guess, denoted as starting point $\vec{p_0}$, for PSO. To ensure a wide search space while minimizing resource usage for achieving an optimum within a reasonable timeframe, the particle count is set to 16, and a mesh accuracy of 3 is chosen with conformal variant 0 meshing for FDTD. Broadband simulations are conducted within a range of 1450 nm to 1650 nm. The input consists of ten modes calculated at different positions, distributed as Chebyschew nodes. Through this process, the following parameters have been identified:

$$\alpha_{PSO} = (15 \pm 0.2)°, \quad L_s^{PSO} = (8.0 \pm 0.5)\mu\mathbf{m} \tag{4.2}$$

The uncertainty was estimated from the final distribution of the particles. this result for α is closely in agreement with that obtained from the TMM. However, L_s is significantly smaller, as TMM does not account for the coupling of input and output bends and the curvature was assumed to be circular.

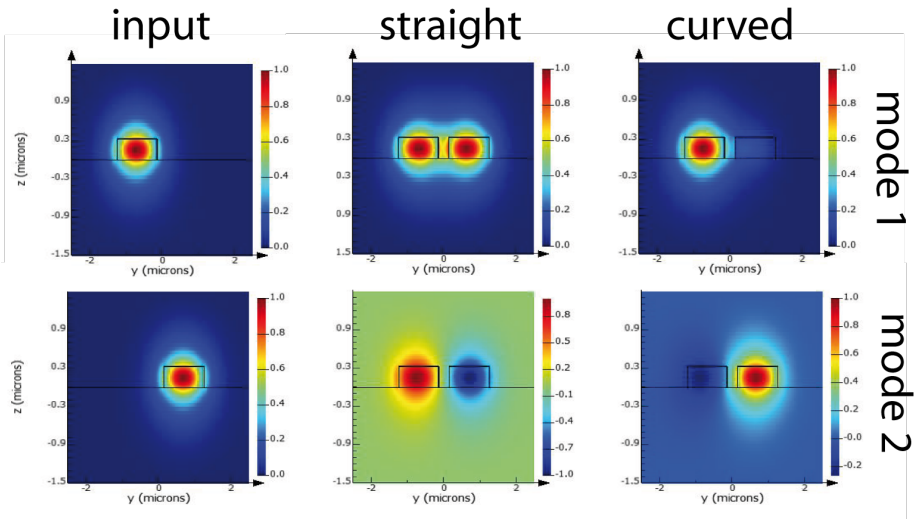

Figure 4.2: Real part of $\vec{E}_y$ of the supermodes in different DC sections, obtained with FDE.

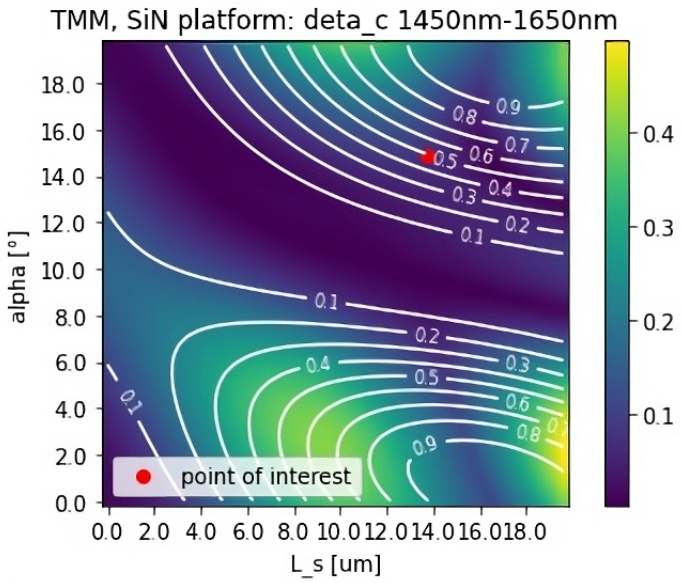

Figure 4.3: Parameter sweep of α and L_s via Transfer-Matrix Method (TMM). The white lines indicate the power splitting ratio η_c, the color indicates its wavelength dependence $\Delta\eta_c$ defined in 2.26.

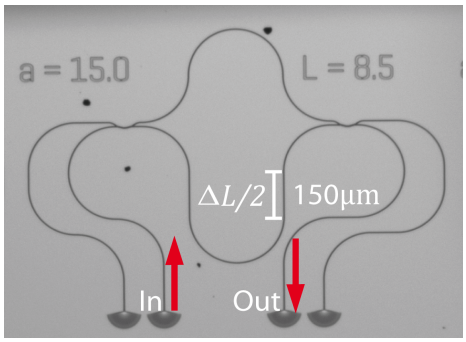

Figure 4.4: MZI under the optical microscope.

4.2 Chip Design

This section illustrates the chips produced with their respective structures. While the PSO simulation uses SiO_2 cladding, actual fabrication uses cured HSQ. Consequently, the agreement of simulation with actual performance is to be tested. To address this, the first chip employs a relatively wide sweep.

Due to the employed fiber arrays, the GCs must be separated by an integer multiple of 127 μ**m**. To reduce errors of the nearest neighboring GCs, the opening angle is decreased from the original 180 to 160 degrees.

In the fabricated chips (except the final broadband sweep), the cladding is applied without structuring. However, there are scenarios where open cladding windows are desired. An example of this is the 3D coupler, which is printed on an open taper. To facilitate this, a specialized cladding layer can be defined, in which all desired structures are buffered by a certain width ($10 \times W$ in this case).

Cascade Sweep

The first chip features casade structures, but the transmission was so weak due to the lack of tapers so no meaningful measurements were possible.

MZI Sweep

The second chip also lacked the taper, but the transmission remained good enough to perform some measurements. However, this chip had been damaged during the inspection at the SEM, so that some structures in the center of the chip no longer functioned. Its sweep Starts from $\alpha = 14.0,\ L_s = 6.0\mu$m to $\alpha = 16.0,\ L_s = 9.5\mu$m with increments of 0.5° for α and 0.5 μm for L_s.

Refined Cascade and MZI Sweep

In total four chips have been designed. The first two were flawed because the taper from the GC to the waveguides was missing. The third chip has a sweep over the cascade structures starting from $\alpha = 14.5,\ L_s = 5.0\mu$m to $\alpha = 15.5,\ L_s = 9.5\mu$m with increments of 0.5° for α and 0.5 μm for L_s. In addition, a sweep over MZIs starting from $\alpha = 14.5,\ L_s = 5.0\mu$m to

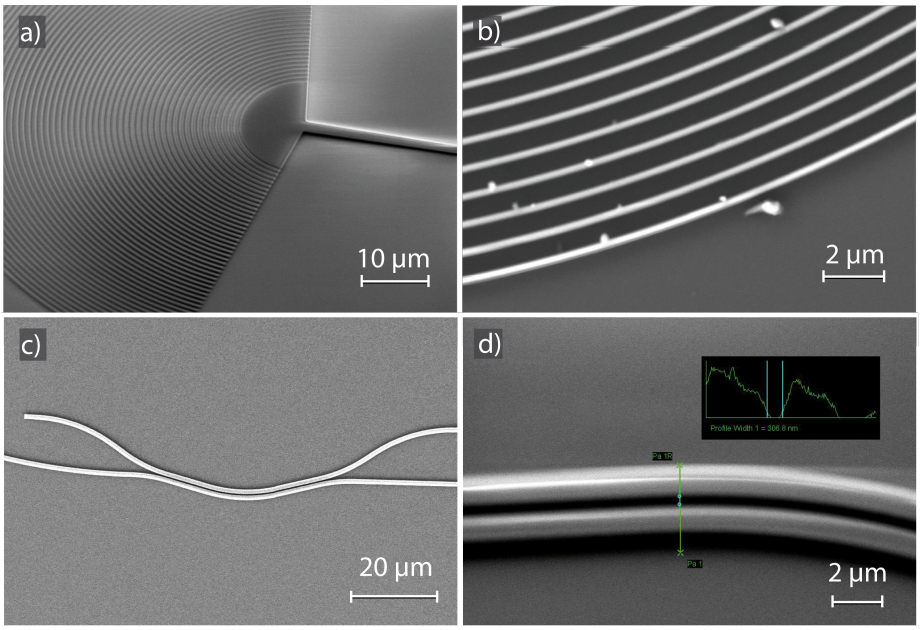

Figure 4.5: Scanning electron microscope (SEM) images of the grating couplers (GC) and directional couplers (DC), a) GC with 160° opening angle, b) dirt particles have been found on some GCs, c) DC from the cascade structure, d) gap measurement.

$\alpha = 15.5,\ L_s = 9.0\mu$m with the same increments is also included as well as grating coupler test structures for calibration. Some structures were not fabricated due to time constraints, and some structures at the edges of the chip were severely damaged, preventing any meaningful measurement.

Broadband MZI Sweep using 3D couplers

The final chip has the fewest structures as it uses the time-consuming MZIs with 3D coupler. These MZIs are built smaller than the previous ones while doubling the path difference to 600 nm. Its sweep ranges from 8.0 μm to 9.0 μm in increments of 0.1 μm for L_s while $\alpha = 15°$ stays constant. In addition, the same MZIs but with GCs are added. The reason for this is on the one hand to check the replicability of the §D coupler results with other couplers and as a back-up in case the production of the 3D couplers has to be postponed due to lack of time. For calibration, the chip features test structures both with 3D couplers as well as GCs.

Meanwhile, more precise FDTD simulations are conducted: these use a mesh accuracy of 8 in the simulation region, along with an additional finer mesh for the coupling sections with a 0.15 μm buffer to fully encompass the gap, which is crucial for coupling. This finer mesh has a maximum grid cell size of $dx = 25$ nm, $dy = 10$ nm.

4.3 Nanofabrication Results

The fabrication outcome is examined using SEM and optical microscopy prior to cladding spin-coating. Special attention is given to grating couplers (GC), in addition to DCs and waveguides. This is due to the fact that the GCs exhibit very fine structures, comparable to typical dose-test structures.

Except for some structures at the edges of the chips, especially the sweep over cascades, the waveguides have been fabricated for most structures without any problems visible in the SEM.

No significant fabrication issues were observed in regard the GCs except for few dirt particles on some GCs (Figure 4.5). This decreases the transmission of the GCs, limiting the interpretability of the cascade measurement, while leaving the extinction ratios of the MZIs unaffected, as errors in the GCs decreases both transmission maxima and minima equally.

No significant fabrication errors were found for the DCs. Additionally, SEM enables intensity profile plotting of the images, which can be used for component size determination. This method determined the gap distance at 306.8 nmand the width at 1.084 μm (Figure 4.5). However, this measurement is highly imprecise, as the intensity profiles do not correspond to the height profiles, necessitating cautious interpretation of these results.

The images give the impression of a smooth surface, but more precise assessments are not feasible due to lack of image contrast. Atleast one measure to address charging of the sample could involve using a adhesive with silver instead of the used carbon pads, which would enhance conductivity and enable more accurate imaging without the electron beam being deflected that much.

An alternative method to investigate the surface roughness of the sample is to scan the surface with an Atomic-Force Microscope (AFM). This method yields a sharper resolution and, unlike the SEM, measures the actual topography of the structures. However, this gained accuracy comes at the expense of time since accurate scanning consumes more time. This is a major disadvantage compared to SEM, in this work it is necessary to quickly inspect every structure on the chip for defects.

4.4 Measurement

4.4.1 Grating Couplers

Figure 4.6b depicts the relative transmission and its gaussian fit obtained through the GC test structure after initial calibration. The laser was set to an intensity of 1 mW at 1550 nm. However the photodetector and the Thorlabs power meter registered only (0.90 ± 0.05) mW which corresponds to a loss of (0.46 ± 0.24) dB.

The losses due to intrinsic absorption, due to e.g. rayleigh scattering at inhomogeneities in the material, are relatively low (dB/km order of magnitude) thus cannot be considered as the main cause in this case. Bending of the optical fibers, which was necessary in some cases to interconnect the components on the setup, can lead to radiative losses (macrobending losses). Deformations and damage to the cable at the microscopic level can result in variations of

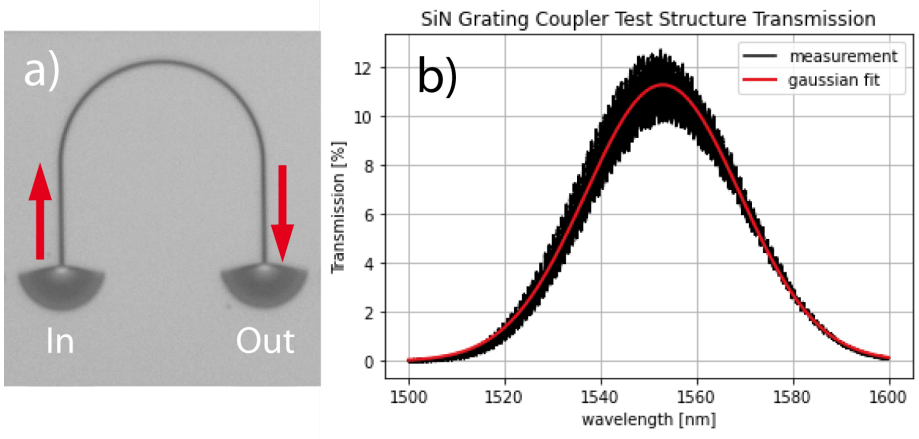

Figure 4.6: a) Simple design for calibration and testing of the GCs. b) Measured transmission spectrum in % with gaussian fit (red).

the refractive index, which additionally contribute to the radiative losses (microbending losses). Another source of error is identified at the fiber connection points. The connectors are not perfectly aligned, resulting in incomplete light coupling, further worsened by surface roughness, damages like scratches, and dust particles. While the fibers were regularly monitored for these defects using an inspection microscope, they could still reside within the fiber and remain undetected during inspection.

The peak transmission of the GC test structure is 11 %, corresponding to a total loss of (9.5±0.41) dB of the test structure. The uncertainty is derived from a min-max estimation based on the measured transmission. To determine the actual insertion loss of an individual GC, only the previously determined total input loss needs to be subtracted from it and then divided by two. Consequently, an insertion loss of (4.56 ± 0.12) dB per GC at 1550 nm is obtained. Its error margin has been determined using gaussian uncertainty propagation.

GCs exhibit a trade-off between coupling efficiency and bandwidth. This is due to the fact that light is coupled into the waveguides through diffraction, which requires different grating parameters for each wavelength. Additionally, the alignment of the fiber array has been optimized only for 1550 nm, and an optimal position for a different wavelength would also entail a different bandwidth.

In summary, the GCs are not as effective as anticipated; however, they are sufficiently transmissive to perform meaningful measurements on the structures.

4.4.2 Power Splitting Ratio

Using the measurement results of the MZIs, it is possible to obtain the extinction ratio (dB) from the difference between the maxima and minima (dBm). Using equation 2.34, the power splitting ratio η_c can be calculated from this.. Figure 4.7 shows the sweep over L_s, where 6.5 μm and 7.0 μm were defect and thus not included. The progression of η_c increases up to $L_s = 8.5$ μm where it also has a local minimum in $\Delta\eta_c$. The sweep over the MZIs yielded the best results

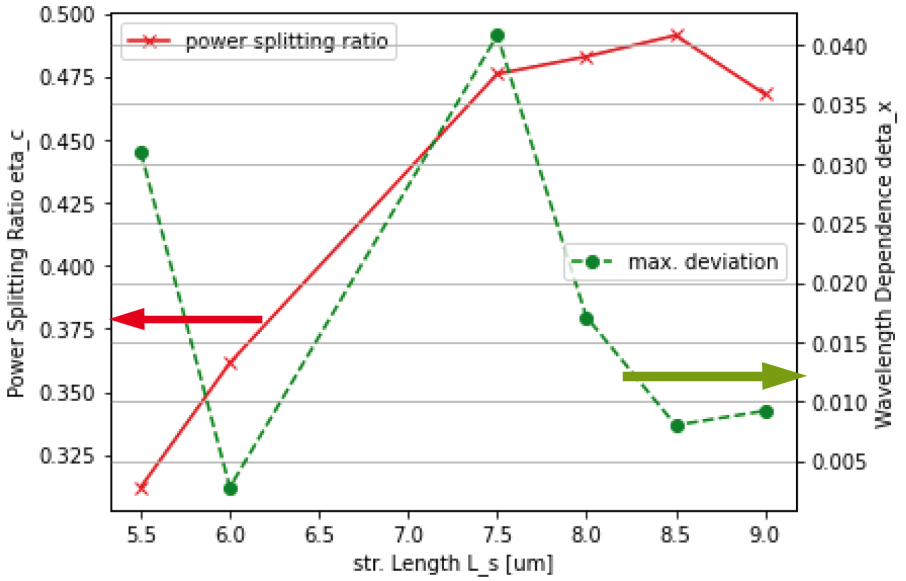

Figure 4.7: MZI sweep from chip 2.

for the following parameters:

$$\alpha = 15^{\circ}, \quad L_s = 8.5\mu\mathbf{m} \tag{4.3}$$

Figure 4.8 illustrates in a) the measured spectrum in dBm and in b) the ERs in dB of the MZI, calculated from the differences of the maxima and minima, from which the power splitting ratio η_c (Figure 4.9) is calculated using Equation **??**.

The uncertainty of the transmission is etstimated to be 0.2 dBm, primarily caused by noise at the photodetector and the environment. Figure 4.9 also presents the outcome of the exact FDTD simulation, where a cladding refractive index of $n = 1.39$ for cured HSQ was used to facilitate more precise simulations. Cured HSQ has a slightly lower refractive index than SiO_2 (see [18]). As an approximation, this refractive index has been considered constant for the investigated range, which could potentially make the simulation results less accurate at the edges of the spectrum. Simulation and experiment are in close agreement, thus presenting acceptable outcomes for the DCs. For the purposes of this work, it can be assumed that FDTD simulations offer a suitable solution for analyzing this type of problem. If the trend of the FDTD results aligns with the actual performance beyond the laser's bandwidth, this implies a 0.5 dB bandwidth of potentially up to 300 nm, ranging from 1420 nm to >1700 nm.

The 0.5-dB bandwidth defines the range between the eta of a 3.5 dB splitter and a 2.5 dB splitter. This metric is commonly used in literature to determine a suitable measure for bandwidth.

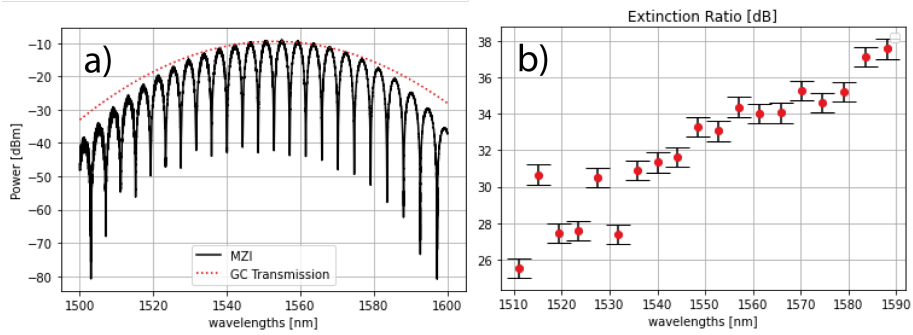

Figure 4.8: Measured transmission result for $L_s = 8.5$ μm and $\alpha = 15°$.: a) MZI (black) and GC (red) transmission. b) ERs obtained from minima and maxima.

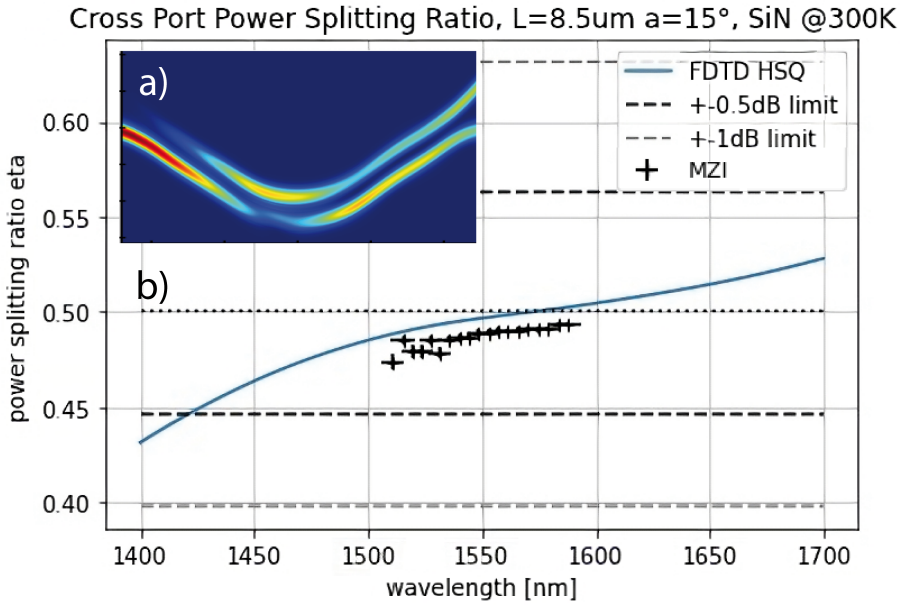

Figure 4.9: Results for $\alpha = 15°$ and $L_s = 8.5\mu$m: a) Simulated intensity at the mid-height of the waveguides @1550 nm. b) η_c obtained from the MZI's ERs (black) compared to those obtained from the simulation (blue).

4.4.3 Insertion Loss

Cascade

Figure 4.10 depicts the cascade structure and its port allocation in (a), while (b) illustrates the losses of the respective ports, calculated from the output power at 1550**nm** and an input power of 0.9**mW**.

The IL of a DC with $\alpha = 15°$ and $L_s = 9.0\mu\mathbf{m}$ determined from the slope of the linear fit is:

$$a_I = (0.39 \pm 0.84)\mathbf{dB} \tag{4.4}$$

The measurement posed challenges due to the sensitivity of the GCs to alignment errors in the fiber array, resulting in significant variations in the measured transmissions. Even slight changes in the position of the fiber array led to different outcomes. In this regard, an error of approximately 1 dB per port was estimated in b).

Additionally, the size of the structure renders it particularly susceptible to errors. Even small dirt particles present on either the waveguides or the GCs can significantly affect the transmission, rendering the measurements incapable of obtaining meaningful slopes. Unfortunately, this problem has occurred in this case for the DC parameters of interest $\alpha = 15°$ and $L_s = 8.5\mu\mathbf{m}$, which is why the nearest neighboring structure with $L_s = 9.0\mu\mathbf{m}$ has been used.

MZI and GC

An alternative method for determining the ILs involves calculating the difference in transmissions between the GC test structures and the MZIs. Half of this difference corresponds to the IL of a DC, assuming negligible propagation and bending losses. As the same issue persists here, where the measurements on the GC test structures do not precisely have the same GCs and fiber array positions as the MZIs, an assumption is made that all DCs exhibit the same IL. Thus, the differences can be calculated for all MZIs, and subsequently, the mean IL can be determined to:

$$\bar{a}_I = (0.36 \pm 0.19)\mathbf{dB} \tag{4.5}$$

Whose uncertainty corresponds to the statistical error of the mean.

4.4.4 Cladding Comparison

The power splitting ratio has also been measured for both with and without cladding. The results for $L_s = 8.0$ μm and $a = 9°$ highlight the significant influence of the cladding on the coupling behavior. The simulation roughly agrees with the measurements here, but not as closely as in the results with cladding. A main cause can be identified: for the simulation without cladding, a refractive index of one (vacuum) was used, while the actual refractive index, that of air, is slightly higher. As seen in the figure, uncertainties are larger in measurements without cladding due to weak extinction ratios, causing the 0.2 dB error induced by the photodetector noise to proportionally increase.

The significant difference of 0.07 @1550 nm between the exact FDTD simulation with SiO_2 cladding and the measurements is also notable. They are roughly consistent in terms of shape, but this highlights the significant impact

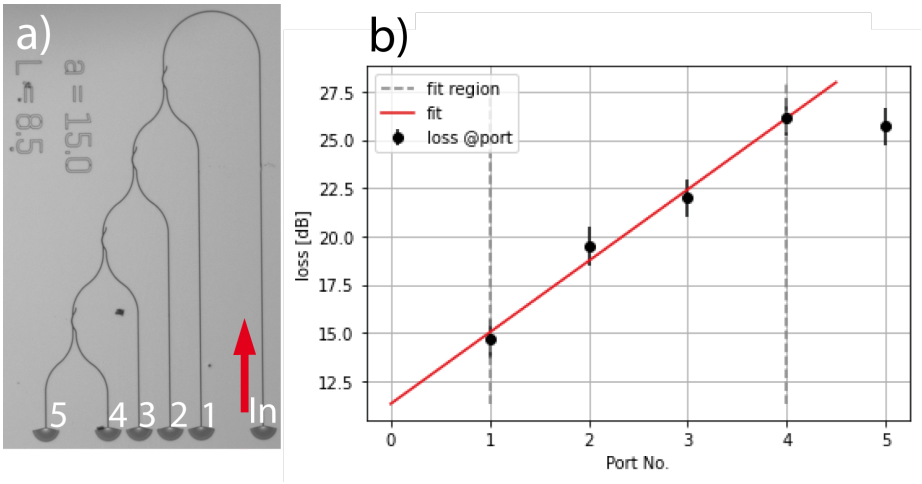

Figure 4.10: a) Cascade structure design under the optical microscope. b) Losses at the ports for $\alpha = 15°$ and $L_s = 9.0\mu\mathbf{m}$ with linear fit (red).

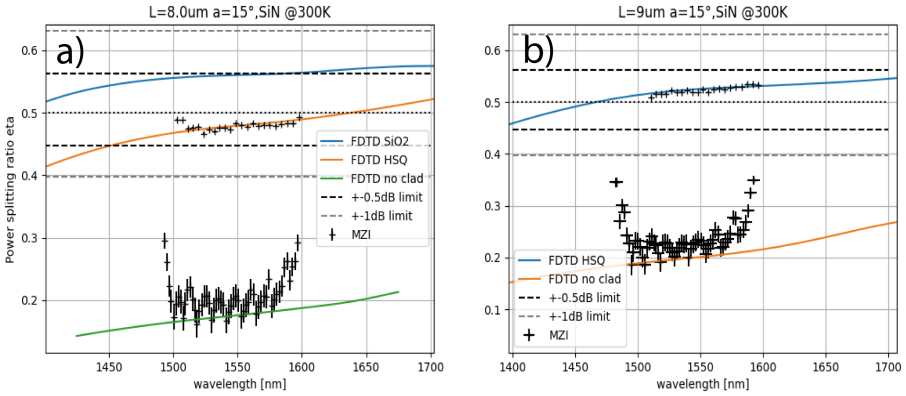

Figure 4.11: Comparison of simulated η_c for $L_s = 8.0\mu\mathbf{m}$ on the left (a) and $L_s = 9.0\mu\mathbf{m}$ on the right (b), with different cladding materials. Experimental η_c from the extinction ratios (ERs) of MZIs with HSQ cladding are shown in black.

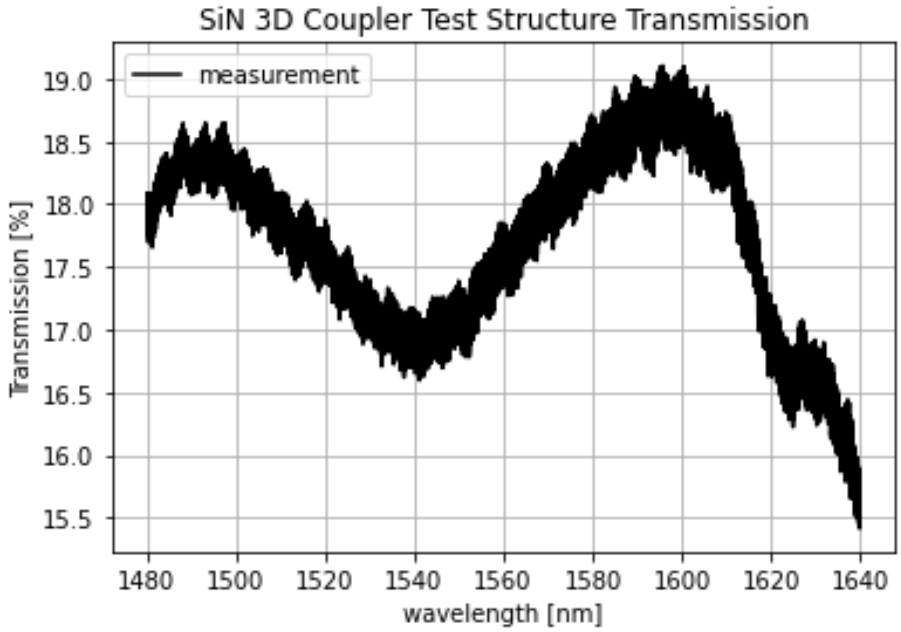

Figure 4.12: Relative tranmission through the §D coupler calibration structure.

of the refractive index of the cured HSQ cladding on the device performance. It is therefore crucial to know the refractive index of the cladding before the optimization process.

4.5 Broadband Measurements

The limited transmission bandwidth of the GC constrains measurements to a range of at most 1500 to 1600 nm. To address this limitation, 3D couplers are employed here, which use coupling based on refraction with a lens instead of diffraction at the grating. The latest chip, equipped with narrower sweeps and featuring 3D couplers, now allows the use of the full tunable laser bandwidth from 1480 nm to 1640 nm.

3D Coupler Test Structure

First, the 3D coupler calibration structure was measured (Figure 4.12). The transmission exhibits wavelength independence across the entire range of the tunable laser, as expected from the 3D couplers. With a transmission of XXX, it surpasses the peak transmission of the grating couplers used in this study. However, an issue has been identified: the maxima of the transmission in the MZIs are significantly better than those of the test structure. One potential reason could be misalignment between the 3D couplera and the input waveguides. The printing process is less precise compared to the scale considered here. Additionally, factors affecting the waveguides may have considerably deteriorated propagation losses, such as metal particles being deposited on it due

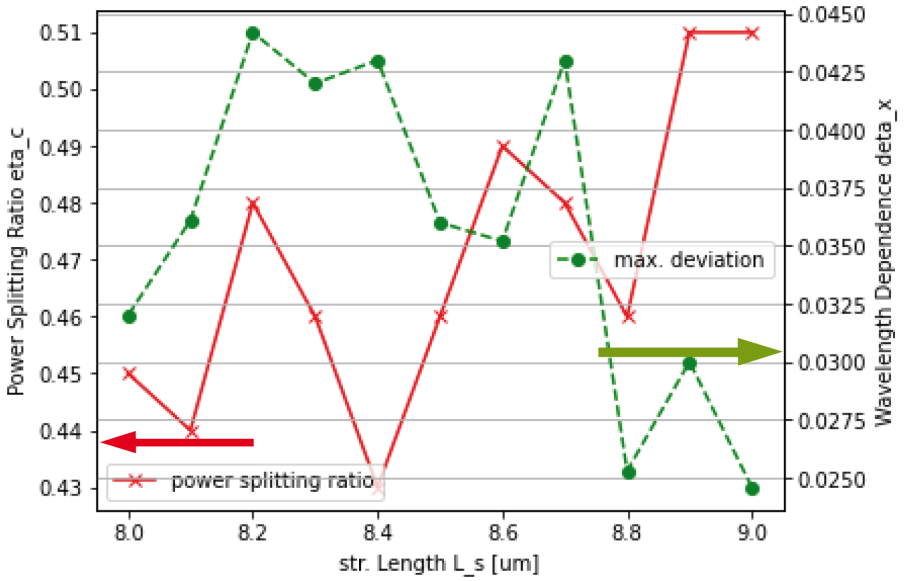

Figure 4.13: The measured power splitting ratios η_c (red) and their maximum deviation $\Delta\eta_c$ (green) for the MZIs from the final chip swept over L_s.

to problems with the RIE machine, which will be discussed later.

MZI

Figure 4.13 illustrates the trend of the power splitting ratio and its wavelength dependence $\Delta\eta_c$ of a sweep across the L_s parameter ranging from 8.0 to 9.0 μm in increments of 0.1 μm. To reduce fabrication time due to the time consuming 3D coupler printing, only $\alpha = 15°$ has been considered.

The results for $L_s = 8.5$ μm (Figure 4.14c) compared with the simulation roughly agrees with the previous findings with GCs, however, it is evident that the power splitting ratio deviates more significantly from the simulation. In this sweep, a relatively thin layer thickness of 124 nm has been applied. The reason is that for cladding-free windows for the 3D coupler, structuring via EBL is required, which demands thinner layer thicknesses and more fabrication constrains compared to the previous process, in which only HSQ was applied via spin coating and then cured. The starting material for the cladding is SX AR-N 8250.03 (also known as Medusa 82), a negative resist by the manufacturer Allresist based on HSQ, which then cured after development with AR 300-44 (TMAH based solution).

Another factor contributing to the deviation between the measurement and simulation, especially at the edges far from 1550 nm, is the cladding index used in the simulation for cured HSQ, which is approximately treated as constant across the investigated range.

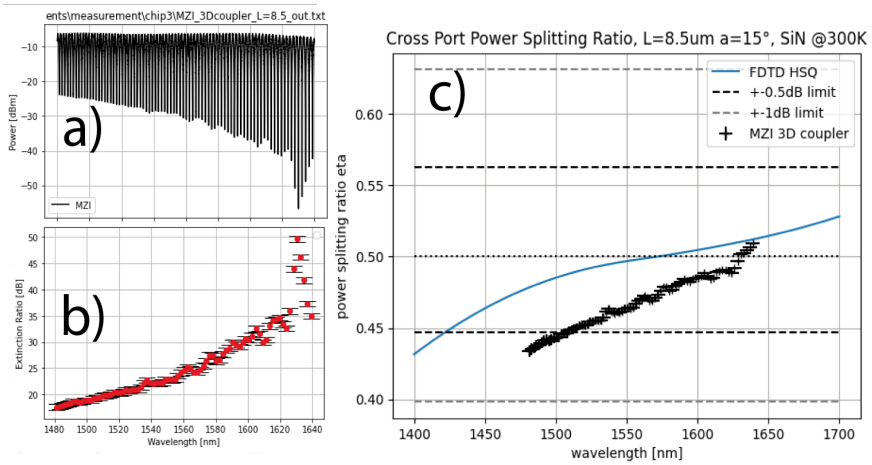

Figure 4.14: Results for $L_s = 8.5\ \mu$m and $\alpha = 15°$: a) measured output power, b) calculated ERs from maxima and minima, c) power splitting ratio measurement (black) and FDTD simulation (blue).

Possible Problems during Etching

The fabrication was carried out under challenging conditions. Particularly, the reactive ion etching posed difficulties due to damage on the carbon plate, exposing small metal surfaces. This could lead to the deposition of metal particles on the surface during etching. Such an occurrence could have detrimental effects on the propagation losses of the waveguides, especially if one of the arms of the MZIs is affected, significantly distorting the ERs. Luckily, no significant transmission drops were observed. The 3D couplers efficiently couple light into the structures, even outperforming their GC counterparts.

Optimal Parameters

he best result was achieved with the following parameters:

$$L_s = 9.0\mu\mathbf{m}, \quad \alpha = 15° \tag{4.6}$$

Figure 4.15 displays its transmitted power and ER. The calculated η_c is shown in Figure 4.16. Here, a 0.5 dB bandwidth of >160 nm can be confirmed for eta_c. iscuss in the next section.

4.6 LNOI and SOI Simulation

Similar toSiN, simulations have also been conducted for the Silicon-on-Insulator (SOI) and Lithium Niobate-on-Insulator (LNOI) platforms, the fundamental procedure here is identical to that for SiN. The objective is to establish the foundations for future devices on these platforms, aiming not only to compare them with SiN-based devices but also to create a diverse repertoire of DCs for various applications across different platforms.

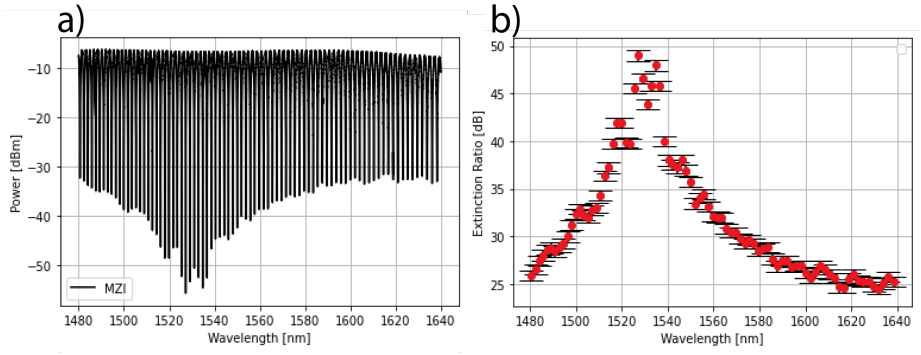

Figure 4.15: The measured power (a) and the derived ERs (b) for $L_s = 9.0$ μm and $\alpha = 15^\circ$ from the final chip with 3D couplers.

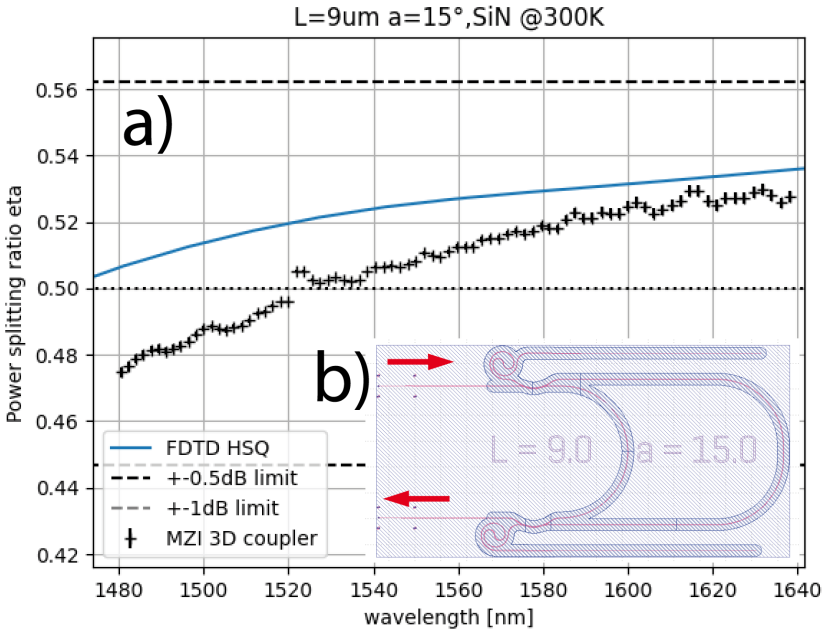

Figure 4.16: $L_s = 9.0$ μm and $\alpha = 15^\circ$ is the best result from the sweep on the final chip: a) power splitting ratio η_c, b) MZI layout with 3D couplers

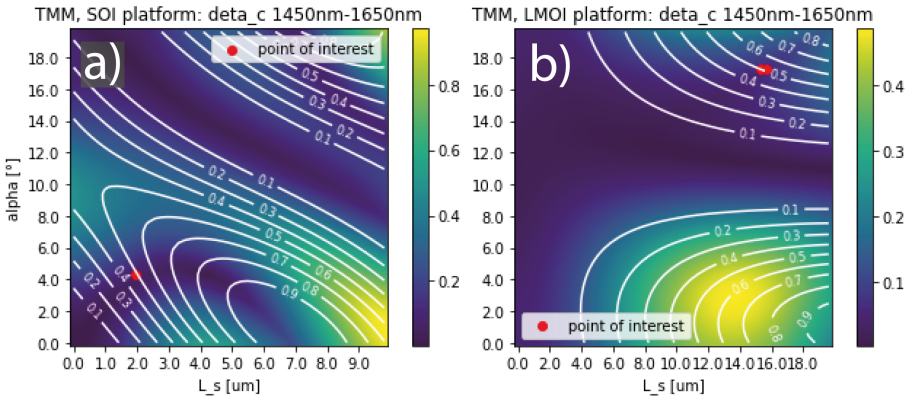

Figure 4.17: TMM results: SOI (a) and LNOI (b)

SOI

$$\alpha_{PSO} = (8.3 \pm 0.5)°, \quad L_s^{PSO} = (1.7 \pm 0.4)\mu m \tag{4.7}$$

LNOI

$$\alpha_{PSO} = (13.2 \pm 0.3)°, \quad L_s^{PSO} = (17.1 \pm 0.5)\mu m \tag{4.8}$$

4.6.1 Chip Design

The sweep on the SOI chip features MZIs equipped with GCs and a path difference of 300 um ranging from $\alpha = 7.3,\ L_s = 2.7\mu$m to $\alpha = 9.3,\ L_s = 1.3\mu$m with increments of 0.2° for α and 0.2 μm for L_s.

There are not so many MZIs on the LNOI, because they are equipped with 3D couplers here. The fabrication of fully-etched GCs from LNOI platform has not been sufficiently investigated at present. The sweep range contains MZIs with $\alpha = 13.0,\ L_s = 17.7\mu$m to $\alpha = 13.6,\ L_s = 16.8\mu$m with increments of 0.2° for α and 0.3 μm for L_s.

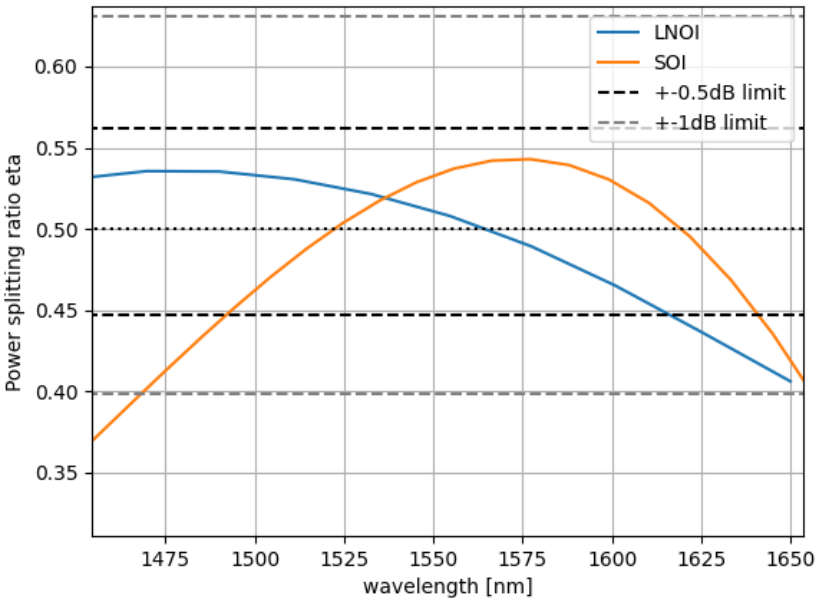

Figure 4.18: Here are the results for SOI (yellow) and LNOI (blue) of the exact FDTD simulation using the parameters from the PSO.

5 | Conclusion

Let us recall the objectives pursued in this study. The aim was to find a method to realize a 3dB-directional coupler (DC) that not only exhibits a wide bandwidth of the power splitting ratio but also maintains low losses. Additionally, the geometry of the coupler was designed to align with the demanding requirements of integrated photonics, e.g. contrains in the waveguide geometry. Let us take an overview of what has been done:

5.1 Summary

In this work, the optimization of the SiN DC geometry, particularly the parameters L_s, representing the length of the straight section, and α, indicating half of the bend angle (Figure 3.1), was conducted. The remaining parameters are either predetermined due to the requirements of the circuits in which they are utilized (such as thickness and etch depth) or have been determined through initial FDE and subsequent TMM analyses, such as width and radius. These initial FDE and TMM sweeps also provided the starting point for PSO algorithm. This algorithm finds the minimum of a given search space, in this case, L_s and $alpha$. The function utilized in this process is FDTD simulations, which return the power splitting ratio η_c and its maximum deviation $\Delta\eta_c$ (Ideally, we aim for an η_c of 0.5 and a deviation of 0).

The result of the optimization is $L_s = (8.0 \pm 0.5)$ μm and $\alpha = (15.0 \pm 0.2)^\circ$. Around these parameters, sweeps of cascade structures were conducted to de-

Device	**Bandwidth[nm]**	**loss[dB]**	**Footprint[μm^2]**
Literature			
SOI, standard[22], [23]	30 ($\pm$1 dB)	n/a	n/a
SOI, Gupta et al. [21]	100 ($\pm$0.5 dB)	0.8	n/a
SOI, Lu et al. [22]	>100 ($\pm$1 dB)	< 0.7	32 $\times$ 1.3
SiN, Li et al. [23]	80 nm ($\pm$1 dB)	0.25	20 $\times$ 5*
This work			
SiN	>160 ($\pm$0.5 dB)	(0.36 $\pm$ 19)	38.6 $\times$ 6.5
SOI (FDTD)	130 ($\pm$0.5 dB)	-	18.0 $\times$ 3.1
LNOI (FDTD)	>200 ($\pm$0.5 dB)	-	47.1 $\times$ 7.3

Table 5.1: Comparison of the measured results with analogous examples from the literature. (*) Estimation obtained from geometry parameters.

termine the losses, and MZIs were used to determine the ERs and subsequently η_c and $\Delta\eta_c$.

The initial sweep over the cascade structures yielded inconclusive results due to weak transmission. However, certain structures from the first MZI sweep provided sufficient transmission to establish a second sweep. This, along with the corrected cascade structures, was fabricated onto a chip containing calibration structures as well. In this sweep, the parameters $L_s = 8.5$ μm and $\alpha = 15°$ exhibit the best performance (Figure 4.9).

With the new cascade structures, it was possible to find a plausible loss of (0.4 ± 0.8) dB for $L_s = 9.0$ μm, but with significant uncertainties. An alternative approach involves comparing the transmission of the GC test structures to that of the MZIs, where an insertion loss of (0.36 ± 0.19) dB per DC was identified. However, it is based on the assumption that the loss is equal for all DCs on the chip.

To explore the promising broadband behavior more comprehensively, 3D couplers instead of the GCs were employed to couple laser light into the structures. These couplers now enable the full usage of the laser's bandwidth from 1480 to 1640 nm. However, the results of the this sweep deviate more significantly from the simulation, e.g. for $L_s = 8.5$ μm (Figure 4.14). The main reason is most likely the thin cladding thickness. The parameters exhibiting the best performance in this case are $L_s = 9.0$ μm, while alpha remains at 15°: Figure 4.161 demonstrates its bandwidth of >160 nm and a splitting ratio of 51% at 1550 nm. The comparison with literature values of DCs with a similar concept in Table 5.1 highlights the achieved the bandwidth.

Finally, the same approach has been applied to other material platforms, specifically silicon-on-insulator (SOI) and lithium niobate-on-insulator (LNOI). Figure 4.18 displays their power splitting ratios (51% for LNOI and 54% for LNOI at 1550 nm). Their chip designs are ready for fabrication.

5.2 Outlook

To test the DCs on both SOI and LNOI platforms, fabrication of sweeps is required. Due to the susceptibility of cascade structures to alignment issues, racetrack resonators can be used as an alternative for loss determination. Employing a sweep across different resonator lengths, in combination with propagation loss measurement, allows determination of the insertion loss of an individual DC. Since the cladding refractive index is crucial for coupling, this needs to be examined more closely for cured HSQ, e.g., using reflectometry.

The wide bandwidth enables the realization of integrated photonic circuits with enhanced performance. As an example, the splitting of light pulses can be mentioned, which is not feasible with conventional DCs due to a broadband requirement. Another potential application benefiting from this improved bandwidth is neuromorphic photonics, where DCs serve as building blocks for modulators enabling matrix-vector multiplications. Integrating these advanced devices into photonic tensor core architectures and spatially multiplexed integrated number-resolving detectors promises the realization of highly efficient, wavelength-independent architectures with remarkably low losses. The method has been applied in a wide range of photonic platforms such as Si, SiN, and $LiNbO_3$, allowing to prove its robustness and accuracy, paving the way for

future investigation focused on exploring alternative optical ranges and more exotic material platforms.

Bibliography

[1] A., Saleh Bahaa E, and Malvin Carl Teich. "Fundamentals of Photonics". John Wiley & Sons, (1991). Ch.9 s.4 "OPTICAL COUPLING IN WAVEGUIDES"

[2] Chrostowski, Lukas, and Michael Hochberg. Silicon Photonics Design: From Devices to Systems. Cambridge University Press, 2015.

[3] Amnon Yariv and Po chiYeh. Photonics: optical electronics in modern communications. Oxford series in electrical and computer engineering. Oxford University Press, NewYork, NY[u.a.], 6.ed.edition, (2007). ISBN0-19-517946-3;978-0-19-517946-0.

[4] Z. Zhu and T. G. Brown, "Full-vectorial finite-difference analysis of microstructured optical fibers," Opt. Express 10, 853–864 (2002)

[5] Snyder and Love "Optical Waveguide Theory", Chapman Hall, London, England, (1983).

[6] A., Saleh Bahaa E, and Malvin Carl Teich. "Fundamentals of Photonics". John Wiley & Sons, (1991). Ch.5 "ELECTROMAGNETIC OPTICS"

[7] Chen, G.F.R., Ong, J.R., Ang, T.Y.L. et al. "Broadband Silicon-On-Insulator directional couplers using a combination of straight and curved waveguide sections". Sci Rep 7, 7246 (2017). https://doi.org/10.1038/s41598-017-07618-6

[8] Kennedy, J. and Eberhart, R. C. Particle swarm optimization. Proceedings of IEEE International Conference on Neural Networks, Piscataway, NJ. pp. 1942-1948, 1995

[9] Eberhart, R. C. and Kennedy, J. A new optimizer using particle swarm theory. Proceedings of the Sixth International Symposium on Micromachine and Human Science, Nagoya, Japan. pp. 39-43, (1995)

[10] Yudong Zhang, Shuihua Wang, Genlin Ji, "A Comprehensive Survey on Particle Swarm Optimization Algorithm and Its Applications", Mathematical Problems in Engineering, vol. 2015, Article ID 931256, 38 pages, (2015). https://doi.org/10.1155/2015/931256

[11] M. Clerc and J. Kennedy, "The particle swarm - explosion, stability, and convergence in a multidimensional complex space," in IEEE Transactions on Evolutionary Computation, vol. 6, no. 1, pp. 58-73, Feb. (2002), doi: 10.1109/4235.985692.

[12] E. D. Palik, Handbook of Optical Constants of Solids (Academic, San Diego, (1985)

[13] Kevin Luke, Yoshitomo Okawachi, Michael R. E. Lamont, Alexander L. Gaeta, and Michal Lipson, "Broadband mid-infrared frequency comb generation in a Si3N4 microresonator," Opt. Lett. 40, 4823-4826 (2015)

[14] D. E. Zelmon, D. L. Small, and D. Jundt. Infrared corrected Sellmeier coefficients for congruently grown lithium niobate and 5 mol. magnesium oxide-doped lithium niobate, J. Opt. Soc. Am. B 14, 3319-3322 (1997)

[15] Helge Gehring, Matthias Blaicher, Wladick Hartmann, and Wolfram H. P. Pernice, "Python based open source design framework for integrated nanophotonic and superconducting circuitry with 2D-3D-hybrid integration", OSA Continuum 2, 3091-3101 (2019)

[16] https://shapely.readthedocs.io/en/stable/manual.html

[17] Holzwarth C., Barwicz Tymon, Smith Henry. (2007). Optimization of hydrogen silsesquioxane for photonic applications. Journal of Vacuum Science and Technology B - J VAC SCI TECHNOL B. 25. 10.1116/1.2787832.

[18] Yang Chang-Chung, Chen Wen-Chang. (2002). The structures and properties of hydrogen silsesquioxane (HSQ) films produced by thermal curing. Journal of Materials Chemistry - J MATER CHEM. 12. 1138-1141. 10.1039/b107697n.

[19] Z. Cui, Nanofabrication: Principles, Capabilities and Limits, Springer, Boston, MA, USA (2008)

[20] Florian Vogelbacher, Stefan Nevlacsil, Martin Sagmeister, Jochen Kraft, Karl Unterrainer, and Rainer Hainberger, "Analysis of silicon nitride partial Euler waveguide bends," Opt. Express 27, 31394-31406 (2019)

[21] R. K. Gupta, S. Chandran and B. K. Das, "Wavelength-Independent Directional Couplers for Integrated Silicon Photonics," in Journal of Lightwave Technology, vol. 35, no. 22, pp. 4916-4923, 15 Nov.15, (2017), doi: 10.1109/JLT.2017.2759162.

[22] Lu, Zeqin & Yun, Han & Wang, Yun & Chen, Zhitian & Zhang, Fan & Jaeger, Nicolas & Chrostowski, Lukas. (2015). "Asymmetric-waveguide-assisted 3-dB Broadband Directional Coupler". CLEO: Science and Innovations, CLEO-SI (2015).

[23] Li, Donghao, Bin Li, Bo Tang, Peng Zhang, Yan Yang, Ruonan Liu, Ling Xie, and Zhihua Li. 2022. "Broadband Silicon Nitride Power Splitter Based on Bent Directional Couplers with Low Thermal Sensitivity". Micromachines 13, no. 4: 559. https://doi.org/10.3390/mi13040559

Acknowledgements

First and foremost, I would like to express my heartfelt gratitude to Professor Dr. Wolfram Pernice for granting me the opportunity to complete my bachelor's thesis within his research group. His guidance and the chance to immerse myself in various facets of integrated photonics have been truly inspiring. Throughout this period, I have not only advanced significantly in my academic pursuits but also experienced personal growth beyond my expectations

I would also like to extend my gratitude towards my supervisor, Dr. Simone Ferrari, for his guidance and mentorship. His dedicated support and infectious enthusiasm for his work have been invaluable to me.

I would also like to thank Linus Krämer for his countless helpful tips, explanations, and assistance that have greatly helped me navigate through various challenges

I would also like to extend my appreciation to Jelle Dijkstra for his introduction to working with the fiber array.

Erklärung

Ich versichere, dass ich diese Arbeit selbstständig verfasst und keine anderen als die angegebenen Quellen und Hilfsmittel benutzt habe.

Heidelberg, den 28. August 2023,

Vincent Leon Spreter